

Global aerosol typing classification using a new hybrid algorithm utilizing Aerosol Robotic Network data

Xiaoli Wei^{1,2}, Qian Cui⁵, Leiming Ma¹, Feng Zhang^{2,3}, Wenwen Li^{2,3}, Peng Liu⁴

¹ Shanghai Meteorological Service 200030, China;

² Shanghai Qi Zhi Institute, Shanghai, 200232, China;

³ Department of Atmospheric and Oceanic Sciences & Institute of Atmospheric Sciences, Fudan University, Shanghai, 200438, China;

⁴ School of Atmospheric Science, Nanjing University of Information Science and Technology, Nanjing 210044, China;

⁵ Caidian Meteorological Service, Wuhan, 430000, China

Correspondence to: Feng Zhang (fengzhang@fudan.edu.cn)

Abstract

Aerosols have great uncertainty owing to the complex changes in their composition in different regions. The radiation properties of different aerosol types differ considerably and are vital in studying aerosol regional and/or global climate effects. Traditional aerosol-type identification algorithms, generally based on cluster or empirical analysis methods, are often inaccurate and time-consuming. In response, our study aimed to develop a new aerosol-type classification model using an innovative hybrid algorithm to improve the precision and efficiency of aerosol-type identification. This novel algorithm incorporates an optical database, constructed using the Mie scattering model, and employs a random forest algorithm to classify different aerosol types based on the optical data from the database. The complex refractive index was used as a baseline to assess the performance of our hybrid algorithm against the traditional Gaussian kernel density clustering method for aerosol type identification. The hybrid algorithm demonstrated impressive consistency rates of 90%, 85%, 84%, 84%, and 100% for dust, mixed-coarse, mixed-fine, urban/industrial, and biomass burning aerosols, respectively. Moreover, it achieved remarkable precision, with F-score and accuracy scores of 95%, 89%, 91%, and 89%. Lastly, a global map of aerosol types was generated using the new hybrid algorithm to characterize aerosol types across the five continents. This study utilizing a novel approach for the classification of aerosol will help improve the

31 accuracy of aerosol inversion and determine the sources of aerosol pollution.

32 **Keywords:** Aerosol typing classification, Hybrid algorithm, Complex refractive index,
33 AERONET

34 **1. Introduction**

35 Atmospheric aerosols are tiny solid or liquid particles suspended in the atmosphere.
36 Aerosols indirectly affect the energy budget and water cycle of the earth's gas system
37 by absorbing and scattering solar radiation or by changing the optical properties and
38 life cycle of the cloud as condensation nuclei of cloud droplets (Redemann et al. 2000;
39 Ramanathan et al. 2001). Additionally, desert dust, biomass smog, and anthropogenic
40 emissions of air pollutants can affect visibility, air quality, and human health (Tong et
41 al., 2017; Siomos et al., 2020). Evaluating the impact of aerosols on radiative transfer
42 is complex, primarily because of the uncertainty of radiative forcing caused by the high
43 spatiotemporal dynamic variation of aerosol optical and physical characteristics in
44 different regions (Kaskaoutis et al., 2011; Che et al., 2018; Elham et al., 2023). The
45 aerosol type embodies the long-term average physicochemical properties of aerosols in
46 a certain area (Kiehl & Briegleb, 1993; Lu et al., 2023). Therefore, accurate
47 identification of aerosol types can drive the study of the climatic effects of aerosols,
48 tracking and control of environmental pollution sources, and precision of radiation
49 transmission models.

50 Aerosol types are defined based on the radiation properties of different aerosol
51 types owing to the large variation in their optical, physical, and chemical properties.
52 Currently, aerosol types are classified by two ways by using the traditional clustering
53 algorithms (Kumar et al., 2018). First, based on different sources and properties at
54 different observation points worldwide, aerosols are classified as follows: dust aerosols
55 from deserts, biomass combustion aerosols from forests or grasslands, and
56 urban/industrial (U/I) aerosols from fuel combustion in densely populated urban areas
57 (Dubovik et al., 2002; Pawar et al., 2015; Yousefi et al., 2020). Second, based on the size
58 of the radiation absorption rate, aerosols into four categories: carbonaceous (fine-

59 absorbing mode), soil dust (coarse absorption mode), sulfates (nonabsorbing fine-
60 grained mode), and sea salt aerosols (nonabsorbing coarse-grained mode) (Levy et al.,
61 2007). The first classification, widely used for aerosol retrieval and common in research,
62 categorizes aerosol types based on optical properties observed at ground stations. This
63 forms a two-dimensional identification space for clustering, while the second approach
64 specifically subcategorizes anthropogenic aerosols. Many combinations of optical
65 properties and parameters are available, such as $EAE_{440-870nm}$ (extinction angstrom
66 exponent) vs. SSA_{440nm} (single-scattering albedo), $AAE_{440-870nm}$ (absorption angstrom
67 exponent) vs. $EAE_{440-870nm}$, $AAE_{440-870nm}$ vs. FMF_{550nm} (fine mode fraction), and
68 SSA_{440nm} vs. $EAE_{440-870nm}$ (Lee et al., 2010; Shin et al., 2019; Choi, et al., 2021). Various
69 studies have highlighted the importance of selecting appropriate aerosol properties for
70 accurate aerosol type identification (Giles et al., 2012; Che et al., 2018).

71 Among the aerosol-type classification methodologies developed, those using
72 threshold and empirical analyses have the greatest potential for large-area and fixed-
73 period applications (Eck et al., 1999; Omar et al., 2005; Yang et al., 2009). Traditionally,
74 the aerosol-type classification algorithm mainly distinguishes different aerosol types
75 based on their optical properties and determines the threshold of their optical properties
76 based on clustering. However, the composition of aerosols changes rapidly with time
77 and location, owing to the combined influence of natural conditions and human
78 activities (for example, tornadoes and various anthropogenic activities) (Sheridan et al.,
79 2001). Unfortunately, determining aerosol types accurately and rapidly is a challenge
80 when using traditional methods (Bahadur et al., 2012; Shin et al., 2019; Lin et al., 2021).
81 Nevertheless, with advancements in data science, artificial intelligence techniques have
82 aided the accurate and rapid recognition of different aerosol types.

83 Artificial intelligence algorithms can receive multiple aerosol characteristic
84 parameters as input, thus preventing the sole reliance of aerosol classification on a
85 limited number of features (Li et al., 2022; Wang et al., 2023). For example, Boselli
86 (2012) performed a k-means clustering analysis of single scattering albedo (SSA),
87 aerosol optical depth (AOD), electrical asymmetry effect (EAE), and asymmetry
88 parameter (g) datasets for the central Mediterranean Sea for the classification of aerosol

89 into four: dusty, continental, oceanic, or mixed aerosols. Nicolae (2018) developed a
90 neural network algorithm to estimate the aerosol typing of Lidar data and Hamill (2016)
91 introduced the Mahalanobis Distance for aerosol classification to determine a specific
92 aerosol type for each reference cluster. Li (2022) generated spatial contiguous aerosol
93 type map in China with an empirical aerosol type retrieval algorithm. Overall, limited
94 information on the optical properties of aerosols can reasonably determine the type of
95 aerosol (Hamill et al., 2016). However, some challenges remain in identifying aerosol
96 types through machine learning. First, the amount of valid ground aerosol property data
97 that can be used for training is less due to cloud removal and quality control. Second,
98 the accuracy of machine learning depends on the labeled aerosol typing dataset, and
99 finding a suitable classification method to classify the dataset is challenging. Third,
100 evaluating the accuracy of the final trained model is also tedious (Zhang & Li, 2019;
101 Siomos et al., 2020; Choi, et al., 2021a,b)

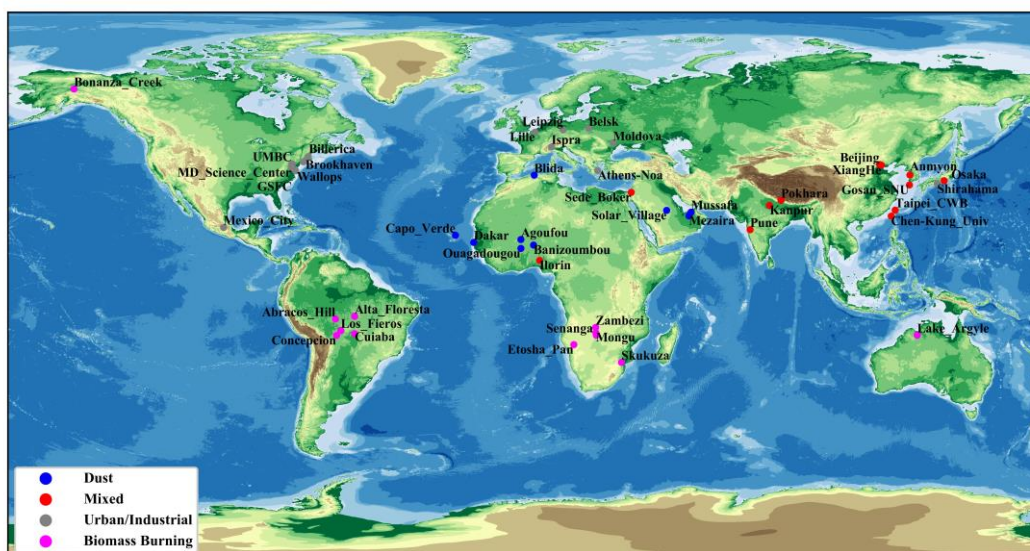
102 The traditional aerosol type identification methods are easily limited by time and
103 space, and most of them only classify aerosol types using two optical property
104 parameters, limiting the complete characterization of aerosols. Considering these
105 limitations, we aimed to (1) develop a new algorithm that can accurately and quickly
106 identify aerosol types to overcome existing problems such as low accuracy, insufficient
107 data, and difficulty in setting labels; (2) investigate the characteristics of the regional
108 spatial distribution of global aerosol types obtained using the new machine learning
109 algorithms, considering the large regional differences in aerosol types. To achieve this,
110 we propose a new aerosol-type classification algorithm based on a Gaussian cluster and
111 random forest algorithm to generate an aerosol-typing map over several representative
112 regions of the world.

113 **2. Study area and data**

114 Figure 1 illustrates the research area and the distribution of the Aerosol Robotic
115 Network (AERONET) sites, strategically encompassing major global regions to
116 validate the universality of the research algorithm. The study utilized 47 marked aerosol
117 sites across five continents, leveraging them to train and validate the machine learning

118 approach based on a comprehensive literature review. The 47 sites represent different
119 aerosol-type properties of different aerosol source regions, including dust, mixed
120 (mixed coarse and mixed fine aerosols), U/I, and biomass burning (BB) aerosols (Table
121 1 and Figure 1). Marine aerosols were not considered because their low optical
122 thickness values (generally <0.4) can result in a less valid data scale that would not
123 meet the study requirements. Here, the aerosol source region refers to the area affected
124 by one dominant emission source, where the aerosol types are fixed and not easily
125 confused (Giles et al., 2012; Hamill et al., 2016). Table 2 presents the optical properties
126 and microphysical characteristic parameters of aerosols at four bands of AERONET
127 (440, 675, 870, and 1020 nm). These parameters were used to construct a database of
128 SSA, AOD, and asymmetry parameters. Further, typical sites dominated by different
129 aerosol types worldwide were selected for compositional analysis using the new model.
130 The selected sites are distributed across different regions of the world and represent a
131 specific aerosol-dominated type and aerosol source region.

132 For dust aerosols, five AERONET sites, namely Banizoumbou, Capo_Verde,
133 Dakar, and Ouagadougou in Africa and Solar_Village in West Asia, influenced by the
134 Saharan Desert, were considered. The Dakar and Capo_Verde sites are located at the
135 tip of the Capo_Verde Peninsula—the westernmost part of Africa, bordering the
136 Atlantic Ocean. Despite being oceanic, these two sites are dominated by dust aerosols
137 influenced by aerosol plumes in the Saharan Desert. Meanwhile, the Banizoumbou and
138 Ouagadougou are centrally located in Africa. Here, northeasterly winds in winter and
139 northwesterly winds in summer transport Saharan Desert dust aerosols. For mixed
140 aerosols, the AERONET sites Ilorin, Kanpur, Sede_Boker, and XiangHe were selected.
141 For U/I aerosols, the AERONET sites GSFC, Ispra, Mexico_City, and Moldova were
142 selected. Four AERONET sites, namely, Alta_Floresta, Abracos_Hill, Lake_Argyle,
143 and Mongu, were selected as BB aerosol-dominant sites.



144

145 **Figure 1.** Study area and 47 AERONET sites selected by literature review.

146 **Table 1.** 47 AERONET sites selected by literature review.

Aerosol Type	Sites for Training	Sites for Testing
Dust	Agoufou,Capo_Verde,Dakar,Mezaira, Mussafa,Ouagadougou	Banizoumbou, Solar_Village, Blida
Mixed	Anmyon, Beijing, Chen-Kung_Univ, Ilorin, Kanpur, Sede_Boker, Gosan_SUN, Pune, Taipei_CWB	Osaka, XiangHe, Pokhara
Urban/Industry	Brookhaven,Billerica,Belsk,GSFC,Ispra,UMBC,Lille, Mexcio_City,Moldova,MD_Science_Center,Wallops	Athens_Noa,Shirahama,Lei pzig
Biomass Burning	Abracos_Hill,Alta_Floresta,Cuiaba,Concepcion Los_Fieros,Mongu,Senanga,Skukuza,Zambezi	Bonanza_Creak, Etosha_Pan, Lake_Argyle

147 **Table 2.** The optical and microphysical properties for aerosol type identification.

	Parameters	Variables (band waves)
Optical Properties	Ångström Exponent (AE)	EAE (440-870) ¹
	Aerosol Optical Depth (AOD)	AOD (440,675,870,1020) ¹
	Single Scattering Albedo (SSA)	SSA (440,675,870,1020) ¹
	Asymmetry Parameter	g (440,675,870,1020) ¹
	Imaginary Part of the Complex Refractive Index	REFI (440,675,870,1020) ¹
	Real Part of the Complex Refractive Index	REFR(440,675,870,1020) ¹
Microphysical Properties	Effective Radius	EffRad-F ² , EffRad-C ²
	Standard Deviation of Effective Radius	StaDev-F ² , StaDev-C ²
	Size Distribution	Vol-Con (0.05-15µm)

148

Note: ¹ refers to wavelength in nm; ² refers to different modes; EAE is Extinction Ångström Exponent; REFI is Imaginary Part of the

149

Complex Refractive Index; REFR is Real Part of the Complex Refractive Index; F refers to fine mode; C refers to coarse mode; EffRad is

150

Effective Radius; StaDev is standard deviation; Vol-Con is Volume concentration.

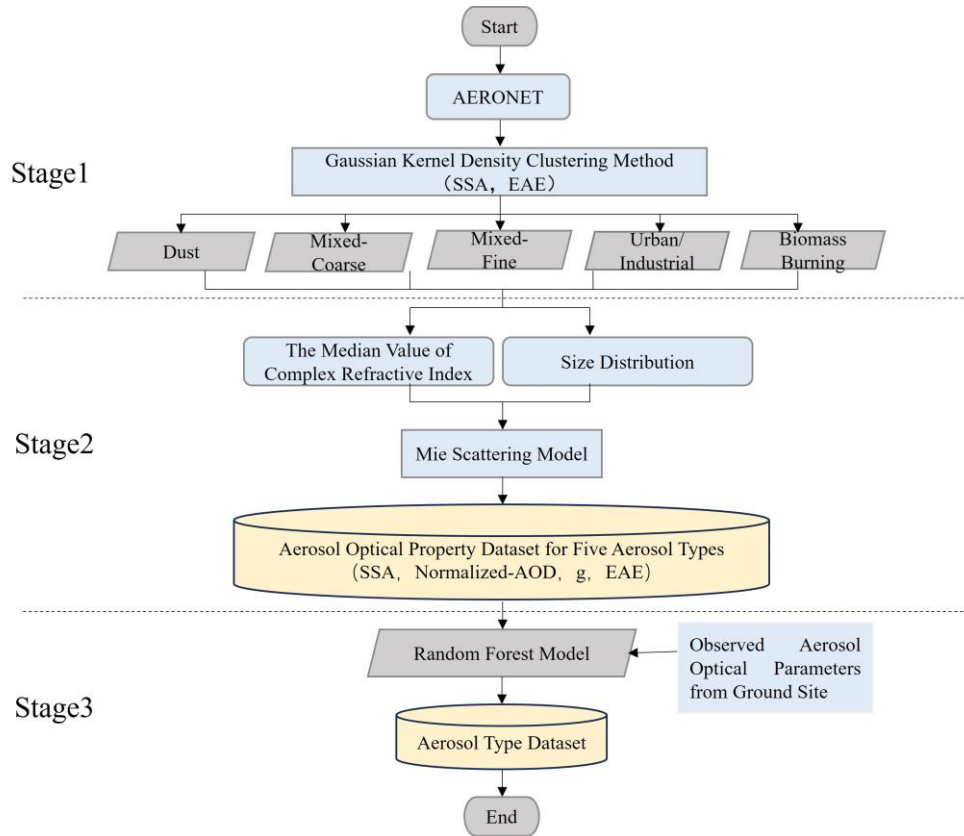
151

3. Methods

152

A new aerosol classification typing hybrid approach that provides insight into

153 spatiotemporal variations in aerosol pollution and climate impacts on a global scale is
154 proposed in this study. In this approach, an aerosol optical properties database using
155 Mie scattering model was built for calculating rapidly unique aerosol-type features.
156 Additionally, the approach introduced, for the first time, the median value of the
157 complex refractive index (CRI) as the criterion for identifying the aerosol type. CRI, a
158 key microphysical characteristic of aerosols, plays a significant role in determining
159 their intrinsic optical properties, such as their ability to scatter and absorb light (Raut
160 and Chazette, 2008). The CRI is also vital for determining aerosols' chemical and
161 physical compositions (Dubovik and King, 2000) and the CRI value is known for pure
162 aerosol components (Nandan et al., 2021). Unlike the mean, the median CRI value is
163 employed in this research for it represents the central tendency of data, especially
164 beneficial in skewed distributions or when outliers are present. This is particularly
165 useful when an average value of a specific aerosol-type might be influenced by the
166 presence of other aerosol types. Moreover, we have selected the aerosol classification
167 based on the source (as described in Section 1), according to the parameters applied in
168 this study and the requirements for AOD retrieval. Figure 2 shows the working
169 flowchart of the new hybrid aerosol-type identification approach, including three stages:
170 aerosol typing preliminary classification, aerosol optical database generation, and
171 global aerosol typing identification. The details of these three stages are as follows.



172

173 **Figure 2.** Flow chart of the new hybrid algorithm in aerosol type identification.

174 **3.1 Aerosol typing preliminary classification (Stage 1)**

175 Stage 1 aimed to solve the problem of obtaining a feature parameter dataset for the
 176 baseline aerosol type. In previous studies, the Gaussian kernel density clustering
 177 algorithm showed great potential for distinguishing the optical properties of different
 178 aerosol types and determining their corresponding thresholds rapidly (Kalapureddy et
 179 al. 2009; Pathak et al. 2012). The high concentration value in each cluster generally
 180 represents the dominant pattern of a specific aerosol type, particularly the data within
 181 the window, taking the cluster centroid as the center and a specific distance as the radius.
 182 Preliminary aerosol-type datasets can be generated by digging deep into the distribution
 183 information of the effective radius, variance, and refractive index of the data within the
 184 window. The spectral absorbability and particle size of aerosols guide the identification
 185 of dust, carbonaceous, or hygroscopic aerosols; SSA indicates the absorption of aerosol
 186 particles; and EAE describes aerosol particle size (Giles et al., 2012). Consequently, in
 187 this study, SSA_{440nm} and $EAE_{440-870nm}$ of 47 AERONET sites and the Gaussian kernel

188 density clustering method was used to estimate the relative densities and determine the
 189 primary patterns of the dominant aerosol types; here, the aerosol type was classified as
 190 a dust aerosol. Eqs. (1) and (2) represent the kernel density and Gaussian kernel density
 191 clustering methods (Rosenblatt, 1956).

$$192 \quad f_{X(v)} = \frac{1}{L} \sum_{i=1}^L k_{\sigma} \left(\frac{\bar{x} - \bar{x}_i}{\sigma} \right), \quad (1)$$

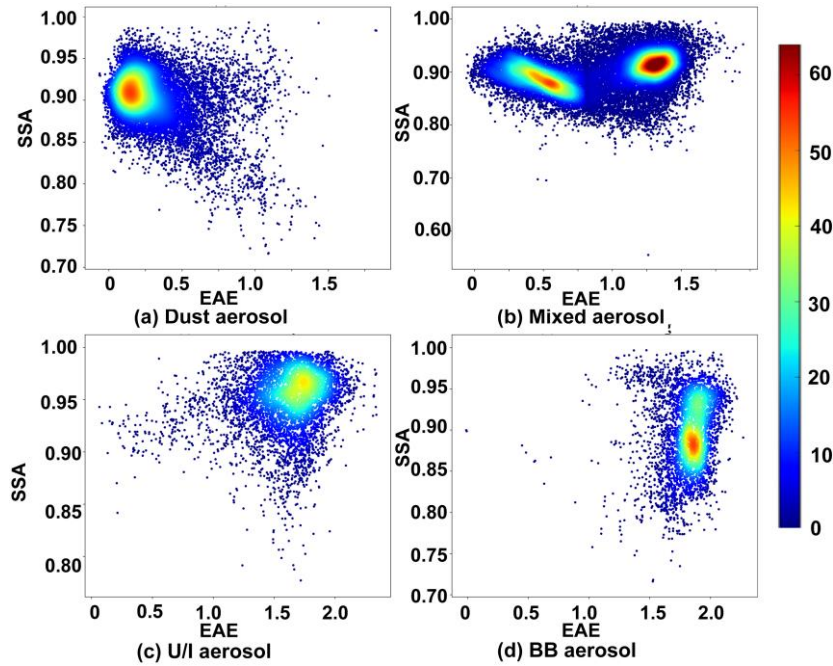
193 where $f_{X(v)}$ denotes the kernel density and k_{σ} indicates the kernel function. x_1, x_2, \dots
 194 x_L are the sample points of independent identical distribution. Mathematically, kernel
 195 functions are symmetric, normalized, and sample-centric when used for density
 196 estimation; this is best described by the Gaussian kernel equation given by Eq. (2).

$$197 \quad k_{\sigma} = \frac{1}{\sqrt{2\pi}\sigma} \exp\left(-\frac{|\bar{x} - \bar{x}_i|^2}{2\sigma^2}\right), \quad (2)$$

198 where σ is the kernel size used as a smoothing factor (Moraes et al., 2021).

199 The mixed aerosols comprised fine- and coarse-mode aerosols, indicated by $EAE >$
 200 0.8 and $EAE \leq 0.8$, respectively. Figure 3 shows the clustering distribution of EAE
 201 and SSA using the Gaussian kernel density clustering method for different aerosol types
 202 at the 47 AERONET sites. For the dust aerosol cluster, the density core area EAE was
 203 $0.1-0.3$, and SSA was $0.89-0.94$, implying that it contained many coarse aerosol
 204 particles with moderate absorptivity. Furthermore, the mixed aerosols had two distinct
 205 centers: one for the coarse-mode aerosols with a median EAE value of 0.4 , indicating
 206 that the cluster contained massive high-absorption aerosols, and the other for fine-mode
 207 aerosols with a median EAE value of 1.3 . Low-absorption aerosols were dominant in
 208 the cluster, similar to U/I aerosols. Additionally, the density core region EAE of U/I
 209 aerosol was $1.5-1.8$, and SSA was $0.94-0.97$, implying the dominance of fine and low-
 210 absorption aerosols. Conversely, BB aerosols had two indistinct centers. This is because,
 211 during biomass combustion, gas and particulate matter emissions are limited by the
 212 combustion conditions, divided into combustion and simmering. Combustion produces
 213 black smoke, and simmering produces white smoke. Combustion, such as burning
 214 flames (grass) with high black carbon content, has a strong absorption capacity,

215 resulting in a low SSA. Simmering, such as burning wood (i.e., trees), tends to be
216 smoldering, lasts longer, has a weaker absorption capacity, and has a higher SSA value.
217 Therefore, despite possessing different absorption characteristics, BB aerosols are
218 defined as one aerosol type with an unseparated center of combustion and simmering.



219

220 **Figure 3.** The clustering distribution of EAE and SSA using the Gaussian kernel density clustering
221 method for different aerosol types.

222 3.2 Aerosol optical database generation (Stage 2)

223 In stage 2, the aerosol optical parameter database was built using the aerosol size
224 distribution parameters, CRI, and Mie scattering model, featuring four major
225 parameters (normalized-AOD, EAE, SSA, and g) at four wavelengths (440, 675, 870,
226 and 1020 nm, respectively). The main reasons for constructing an aerosol optical
227 parameter database instead of using the AERONET data directly are as follows: 1)
228 many data are missed in AERONET, particularly those for sites dominated by biomass
229 combustion, which does not meet the requirements of machine learning methods or
230 traditional aerosol type identification algorithms; 2) Calculating the optical properties
231 of aerosols based on a fixed refractive index can accurately determine aerosol types.
232 Therefore, once the aerosol spectral distribution parameters, such as effective radius,
233 variance, and refractive index, are determined in stage 1, the aerosol optical parameter

234 database can be constructed using the Mie scattering model in stage 2, assuming that
 235 aerosols are spherical particles. The Mie scattering model, known for its simplicity and
 236 practicality, provides an analytic solution to Maxwell's equations for light scattering by
 237 ideal spherical particles. It efficiently depicts the scattering and absorption properties
 238 of aerosols in the atmosphere, serving as fundamental basis of radiative transfer, Lidar,
 239 and optical particle characterization (Ma et al.,2007; Bian et al., 2017; Michael et al.,
 240 1994).

241 **Table 3.** Size distribution parameters of five aerosol types in coarse and fine mode (unit: μm)

Aerosol type	REFF-fine	REFF-coarse	Std-fine	Std-coarse
Dust	0.05-0.42	1.3-2.65	0.5-0.8	0.4-0.7
Mixed-coarse	0.05-0.25	1.25-3.5	0.4-0.8	0.4-0.7
Mixed-fine	0.05-0.27	1.2-4.5	0.3-0.6	0.5-0.8
U/I	0.05-0.26	1.45-3.5	0.3-0.6	0.5-0.8
BB	0.05-0.17	1.35-4.5	0.3-0.5	0.5-0.8

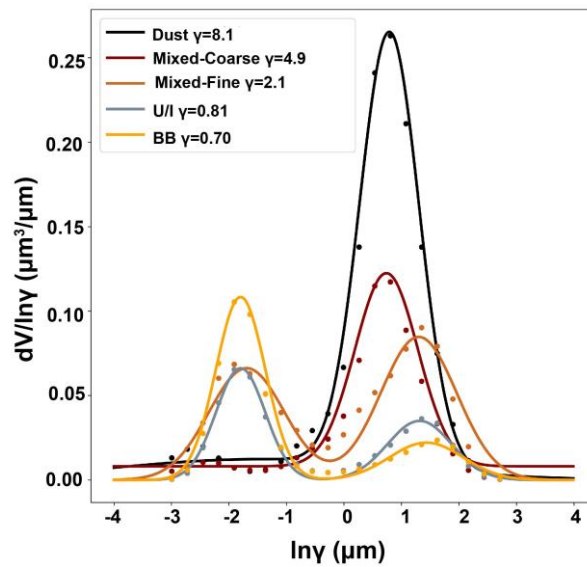
242 Table 3 presents the aerosol size distribution parameters, including the effective
 243 radius and standard deviation range for the five aerosol types in coarse and fine modes,
 244 which were derived from the data window set by the Gaussian kernel density clustering
 245 algorithm. These aerosol size distribution parameters and the median CRI value were
 246 utilized to construct the optical database for the Mie scattering model. Many studies
 247 proven it is a reliable model with the advantage of lower computing load and high
 248 calculation accuracy (Zhao et al., 2008; Fu et al., 2009; Quirantes et al, 2019; Nandan
 249 et al., 2021).

250 The Mie scattering model has various size distribution functions, including log-
 251 normal, power-law, and bimodal log-normal distributions, which describe the aerosol
 252 type. According to the particle radii provided by AERONET, the size distributions of
 253 different aerosol types can be divided into coarse and fine modes. The bimodal log-
 254 normal function [Eq. (3)] is reportedly the most suitable size distribution function for
 255 modeling aerosol particle size distribution (Remer et al., 2009):

$$256 \quad n(r) = \text{const} \times r^{-4} \left\{ \exp\left(-\frac{(\ln r - \ln r_{g1})^2}{2 \ln^2 \sigma_{g1}}\right) + \gamma \exp\left(-\frac{(\ln r - \ln r_{g2})^2}{2 \ln^2 \sigma_{g2}}\right) \right\}, \quad (3)$$

257 where $n(r)$ represents particle count at various radii; constant is obtained by fitting;
 258 While r_{g1} and r_{g2} denote the radii, σ_{g1} , and σ_{g2} are variances for coarse and fine aerosol
 259 modes, respectively; γ , defined by volume distribution, represents the coarse-to-fine
 260 mode ratio in bimodal normal distribution model, fitted using AERONET's volume
 261 distribution data, which averages standard aerosols post-clustering at training sites.

262 Figure 4 shows the volume distributions of five aerosol types, showing dust
 263 aerosols with a peak γ of 8.1 and radii concentrated around 1.5–2.0 μm . Additionally,
 264 the mixed-coarse aerosol with a radius in the range of 0.04–0.2 μm and 4.9 as the
 265 maximum value of γ . The mixed-fine aerosol had two obvious peaks: one with a large
 266 radius, namely the coarse mode, with a radius of 2.2–3 μm and 2.1 as the peak point of
 267 γ ; a second with a small radius of 0.1–0.22 μm and 0.14 as the peak point of γ . Moreover,
 268 the volume distributions of U/I and BB aerosols were similar. Both had a relatively low
 269 range of γ values at large radii and relatively high values at small radii, with peak values
 270 of 0.81 and 0.7 for U/I and BB aerosols, respectively.



271
 272 **Figure 4.** Volume distribution of five aerosol types.

273

274

275

276

277 **Table 4.** Real and imaginary index of CRI for five aerosol types (Bands:440/675/870/1020 nm).

Aerosol Type	Imaginary Index	Real Index
Dust	0.003396/0.000731/0.000639/0.000597	1.4584/1.4681/1.4513/1.4376
Mixed-coarse	0.005766/0.002921/0.002383/0.002043	1.4291/1.4787/1.4745/1.4695
Mixed-fine	0.01075/0.008444/0.009147/0.008955	1.5001/1.5044/1.5056/1.4977
U/I	0.004315/0.004331/0.004419/0.004432	1.4372/1.4280/1.4264/1.4214
BB	0.01828/0.017862/0.018125/0.017858	1.5051/1.5190/1.5228/1.5185

278 The CRI is an inherent optical property of aerosols. Aerosols in the real atmosphere
 279 are usually mixed with different types of particles, which a single refractive index
 280 cannot identify; however, the CRI represents the entire aerosol model in the atmosphere
 281 (Redemann et al., 2000). Ideally, the CRI and aerosol components can be mutually
 282 determined (Wu et al., 2021). The CRI can effectively characterize the main properties
 283 of the aerosols and accurately quantify the difference between aerosol-type
 284 identification algorithms. Table 4 depicts the CRI standard values for the five aerosol
 285 types obtained by calculating the median value of the CRI of the dominant aerosol type
 286 after Gaussian kernel density clustering. These values were used as a baseline for
 287 identifying the aerosol types in subsequent studies. As presented in Table 4, the
 288 minimum imaginary index part is represented by the dust aerosol with CRI of 0.003396,
 289 0.000731, 0.000639, and 0.000597 at 440, 675, 870, and 1020 nm, respectively, owing
 290 to the weakest absorption of dust aerosols. Moreover, the imaginary index part of the
 291 mixed-fine aerosols (0.01) was close to that of the BB aerosols (0.02) because of their
 292 similar absorption properties.

293 Lastly, by fixing the CRI, changing the size distribution, and using the Mie
 294 scattering model, we generated the aerosol optical property database for five aerosols,
 295 including the data for normalized-AOD, EAE, SSA, and g . In the aerosol optical
 296 property database, normalized AOD is the value obtained after eliminating the influence
 297 of the aerosol concentration. The AOD was obtained from the extinction cross section
 298 (C_{ext}) calculated using the Mie scattering model in Eqs. (3) and (4), where β_{ext} is the
 299 extinction coefficient, $n(r)$ is the aerosol spectral distribution, and $N(z)$ is the variation

300 of aerosol concentration with height. Notably, the effect of aerosol concentration needs
 301 to be removed from the AOD when referring to aerosol optical properties. The AOD
 302 was normalized by dividing the aerosol optical thickness at the four wavelengths by the
 303 optical thickness at 440 nm. The other parameters (EAE, SSA, and g) were calculated
 304 using Eqs. (6) – (8).

$$305 \quad \beta_{e/s} = \int_{\gamma_{min}}^{\gamma_{max}} C_{ext/sca} n(r) dr , \quad (4)$$

$$306 \quad \tau_{e/s} = \int_0^{Z_{top}} \beta_{ext/sca} N(z) dz, \quad (5)$$

$$307 \quad EAE_{440-870nm} = -\frac{\ln(\tau_{440nm}) - \ln(\tau_{870nm})}{\ln(440) - \ln(870)} , \quad (6)$$

$$308 \quad SSA = \frac{\tau_s}{\tau_e} , \quad (7)$$

309 and

$$310 \quad g = \langle \cos \Theta \rangle = \frac{1}{2} \int_{-1}^1 p(\cos \Theta) \cos \Theta d \cos \Theta , \quad (8)$$

311 where τ_{440} and τ_{870} are the extinction optical depths of the aerosol at 440 and 870 nm,
 312 respectively, $EAE_{440-870}$ nm is the extinction Ångström index from the 440 to 870 nm
 313 band, and Θ denotes the scattering angle.

314 **3.3 Global aerosol type identification and validation (Stage 3)**

315 In stage 3, the random forest model was introduced to the aerosol-type
 316 identification algorithm. The random forest model is an integrated model based on
 317 classification and regression trees, in which multiple trees are aggregated using
 318 majority voting and averaging for classification and regression (Breiman, 2001). The
 319 model has a high prediction accuracy, excellent tolerance for abnormal values and noise,
 320 and a hard overfit. In a comparison by Fernandez (2014), the random forest algorithm
 321 ranked as the top performer among 179 classification algorithms. In addition, the
 322 evaluation matrix was brought into this study, and it further quantitatively assesses the
 323 performance of the Gaussian density clustering algorithm and the new hybrid algorithm.
 324 The metric indexes include accuracy, recall, precision, and F-scores (Reddy et al., 2022).

325 Here, the indexes are adjusted to micro-precision, micro-recall, micro-F1-score, and
326 accuracy to solve the multi-classification problem. Micro refers to the weighted average
327 of the five aerosol types rather than the arithmetic mean, due to the large difference in
328 sample size among the five aerosol types, the arithmetic mean is highly susceptible to
329 the influence of very large or very few sample size aerosol types.

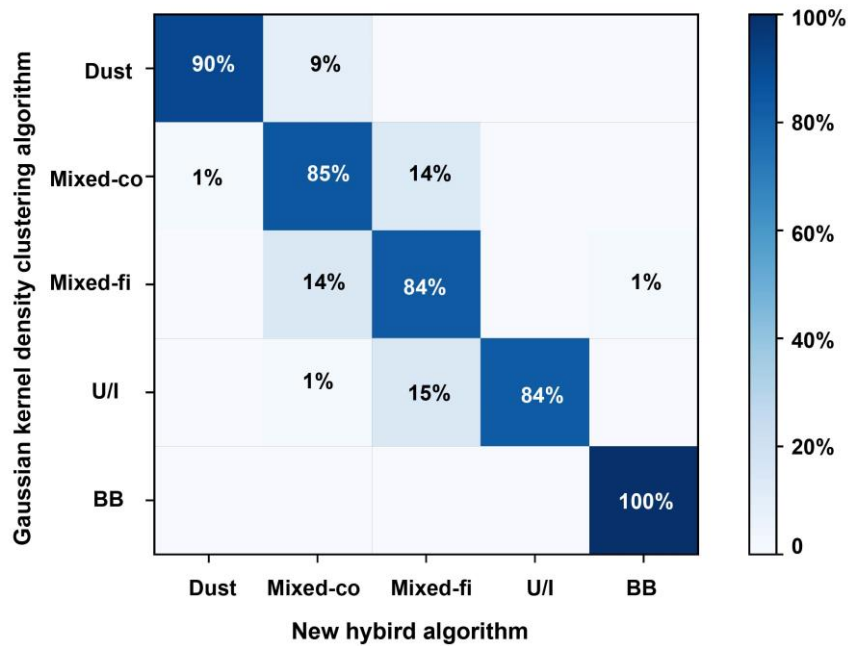
330 The input parameters for random forest model training, including SSA_{440nm} ,
331 SSA_{675nm} , SSA_{870nm} , SSA_{1020nm} , g_{440nm} , g_{675nm} , g_{870nm} , g_{1020nm} , normalized AOD_{675nm} ,
332 AOD_{870nm} , AOD_{1020nm} , and $EAE_{440-870nm}$, were selected from the aerosol optical
333 property database, and the expected output values were the specific aerosol types. The
334 random forest model was optimized, and the parameters were determined using the
335 grid-searching method. The parameters, including `n_estimators` (classifier),
336 `max_features` (maximum feature value), and `min_samples_leaf` (minimum number of
337 samples for nodes), were set as 160, 10, 12, and 12, respectively. Then, based on the
338 trained and optimized model, aerosol typing of any AERONET site in different regions
339 of the world can be identified quickly. Generating the aerosol-type distribution map on
340 a global scale is vital for regional and global climate studies as well as ground remote
341 sensing.

342 **4 Results**

343 **4.1 Algorithm comparison**

344 To demonstrate the effectiveness of the new hybrid algorithm, its performance was
345 compared with that of the Gaussian kernel density clustering algorithm. Figure 5 shows
346 the confusion matrix between the new hybrid and Gaussian kernel density clustering
347 algorithms in identifying aerosol types. The results of the new hybrid algorithm showed
348 90% consistency with that from the Gaussian kernel density clustering algorithm, in
349 delineating dusty aerosols, indicating that its efficiency in identifying dust. For mixed-
350 coarse aerosols, the consistency reached 85%, with 14% identified as mixed-fine
351 aerosols, 1% as dust by the new hybrid algorithm, and 15% as mixed-coarse aerosols
352 by the Gaussian kernel density clustering algorithm. Similarly, for mixed-fine aerosols,

353 both algorithms showed 84% consistency, with 14% identified as a mixed-coarse
 354 aerosol by the new hybrid algorithm and as a mixed-fine aerosol by the Gaussian kernel
 355 density cluster algorithm. Furthermore, both algorithms identified 84% of U/I aerosols
 356 correctly, with the remaining 16% identified as mixed aerosols (fine and coarse). Lastly,
 357 the classification of BB aerosols using these two methods was the same. Overall, the
 358 Gaussian kernel density clustering and new hybrid algorithms were consistent in dust,
 359 mixed-coarse, U/I, and BB aerosol identification.



360

361 **Figure 5.** The confusion matrix between Gaussian kernel density clustering and new hybrid
 362 algorithm.

363 Table 5 shows the metric index value of the random forest algorithm in the new
 364 hybrid algorithm. The micro-precision, micro-recall, micro-F1 score, and accuracy are
 365 0.95, 0.89, 0.91, and 0.89, respectively. These metrics are derived from the core values
 366 of the window, as determined by the Gaussian density clustering algorithm.
 367 Consequently, the strong performance of these indicators further confirms the efficacy
 368 and reliability of the newly developed hybrid algorithm.

369

370

371

372

373 **Table 5.** Matrix evaluation between new hybrid classification algorithm and Gaussian kernel
 374 density clustering algorithm

	Micro- Precision	Micro-Recall	Micro-F1-Score	Accuracy
New Hybrid algorithm	0.95	0.89	0.91	0.89

375 As described in the Methods section, a specific aerosol type theoretically has a
 376 fixed CRI owing to its constant composition. The CRI characterizes the mixture
 377 composition of aerosol particles and is a key parameter controlling the inherent
 378 scattering and absorption characteristics of aerosol particles. To further analyze the
 379 accuracy of the new algorithm, the aerosol CRI was applied as a key criterion for
 380 aerosol identification. The CRI has two parts: imaginary and real. The imaginary part
 381 indicates radiation absorption by aerosols, with a small value signifying a small
 382 absorption. Because the radiation of aerosols is more dependent on the imaginary than
 383 the real part, the imaginary part is essential for inferring the optical properties and
 384 aerosol types. Hence, we compared the real and imaginary parts of the CRI calculated
 385 using the new hybrid and Gaussian kernel density clustering algorithms.

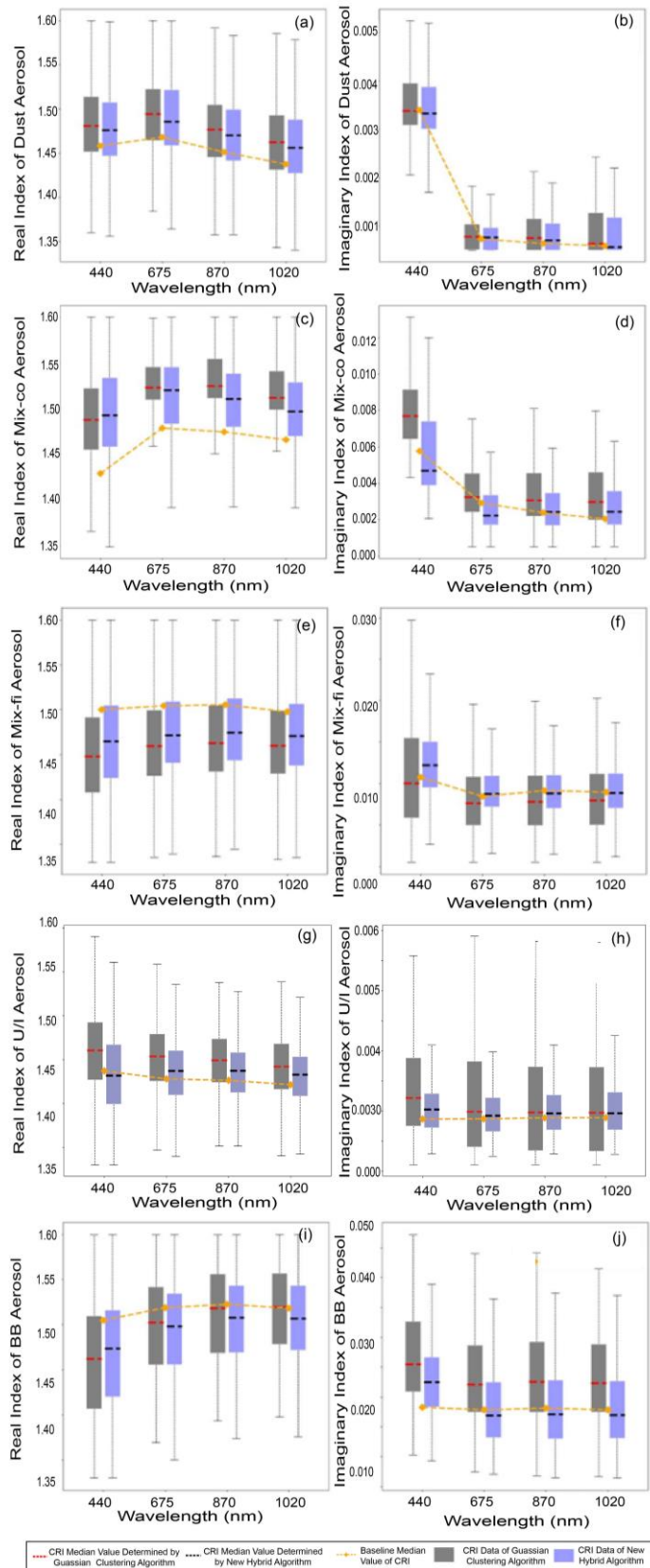
386 Figure 6 shows box plots of the aerosol CRI for dust, mixed-coarse, mixed-fine,
 387 U/I, and BB aerosols using the new hybrid classification and Gaussian kernel density
 388 clustering algorithms. Based on the principle that the CRI of aerosols is fixed under
 389 ideal conditions, the closer the median value of the CRI of the identified aerosol type
 390 is to the median value of the benchmark CRI, the more accurate the identification
 391 method. As shown in Figures 6 (a) and (f), the median values of the CRI real part for
 392 dust aerosol are in the range 1.45–1.53 at four bands, and those of the imaginary part
 393 are 0.003–0.004 at 440 nm; further, the values in other bands decrease rapidly as
 394 wavelength increases. The imaginary part of CRI represents the absorption of light by
 395 the aerosol, with a small absorption indicating strong scattering. The results of the
 396 imaginary part are consistent with the spectral dependence properties of dust-based
 397 aerosols according to the wavelength. This is primarily because dust aerosols,
 398 composed of clay, quartz, and hematite, exhibit strong absorption in the blue band (440
 399 nm) and low absorption in the visible and near-infrared bands. For the dust aerosols,

400 the CRI determined by the two methods did not differ much. However, the median value
401 of the CRI obtained using the new hybrid algorithm was slightly closer to the
402 benchmark CRI than that obtained using the Gaussian kernel density clustering
403 algorithm for dust aerosols. Therefore, the new hybrid algorithm was concluded to be
404 more accurate in identifying dust aerosol.

405 Figures 6 (b) and (g) show the median values of the CRI real part for mixed-coarse
406 aerosol is 1.47–1.55 at four bands using the new hybrid algorithm, but the imaginary
407 part is 0.004–0.009 at 440 nm. However, the real part is 1.44–1.50 at four bands
408 determined by the Gaussian kernel density clustering algorithm, and the imaginary part
409 is 0.006–0.009 at 440nm. The median value of the hybrid algorithm was closer to the
410 baseline median value than that of the Gaussian kernel density clustering algorithm for
411 both the real and imaginary parts.

412 Figures 6 (c) and (h) show the median value of the CRI real part for mixed-fine
413 aerosols determined using the new hybrid and Gaussian kernel density clustering
414 algorithms, which was 1.42–1.51 at four bands. This result is close to the range (1.44–
415 1.52) reported by Wu (2021) in Beijing using a random forest algorithm. The median
416 CRI of the real part at four bands and the imaginary part at the (675–870–1020 nm)
417 bands were close to the baseline median value for the new algorithm. Additionally, the
418 median value of the imaginary part was lower than that of the new hybrid algorithm
419 and further from baseline data for the identifying aerosol type results mixed with 14%
420 coarse aerosols. Mixed coarse aerosols result in weaker absorption. Hence, the new
421 hybrid algorithm performed better at identifying mixed-fine aerosols than the Gaussian
422 kernel density clustering algorithm.

423 Similarly, as seen in Figures 6 (d) and (i), the median value of the CRI real part for
424 U/I aerosol identified using the new hybrid algorithm was 1.39–1.47. This median value
425 was lower than that of the mixed-fine aerosols. This is because the real part indicates
426 the absorption ability of aerosols, and the absorption ability of U/I aerosols was less
427 than that of mixed-fine aerosols. For the imaginary part also, the new hybrid algorithm
428 performed slightly better than the Gaussian kernel density clustering algorithm at the
429 four bands.



431

432

433

434

Figure 6. Box plots of the real index (left) and the imaginary (right) index of the CRI for (a-b) dust, (c-d) mixed-coarse, (e-f) mixed-fine aerosol, (g-h) U/I, and (i-j) BB aerosol identified by the Gaussian kernel density clustering algorithm and new hybrid algorithm, respectively.

435 For BB aerosols, the median value of the real part generated using the new hybrid
436 algorithm differed slightly from that generated by the Gaussian kernel density
437 clustering algorithm. Additionally, the median obtained using the Gaussian kernel
438 density clustering algorithm was closer to the baseline. Furthermore, when analyzing
439 the imaginary part, the new hybrid algorithm performed much better than the Gaussian
440 kernel density clustering algorithm. Even with a 100% concordance rate between the
441 new hybrid and Gaussian kernel density clustering algorithms in identifying BB
442 aerosols, the refractive index still differed. This result indicates that 1% of mixed-fine
443 aerosols classified using the Gaussian kernel density clustering algorithm were
444 correctly identified as BB aerosols by the new algorithm. Overall, these results
445 demonstrate that the new algorithm is reliable.

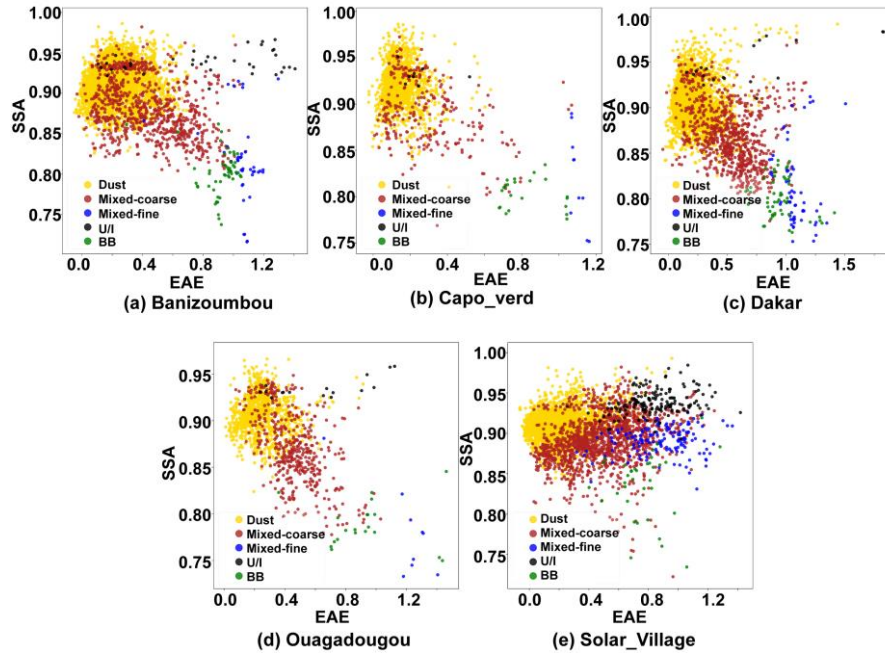
446 Additionally, in this study, the number of 326400 data points from optical
447 parameters database and 98000 observed data for calculation spans from Jan.1st,1993
448 to Dec.31st,2021, passing through Gaussian kernel density clustering algorithm and
449 new hybrid algorithm Python progresses, which is archived on the personal Windows
450 system computer (Intel® Core™ i7-10710U,16G DDR4 2666MHz, 512G PCIE SSD).
451 The computational time for the two algorithms indicates the new hybrid algorithm runs
452 faster than the Gaussian kernel density clustering algorithm with huge quantities of data
453 and trained in advance, which can obtain aerosol type in 20 seconds, in contrast, it will
454 take 30 to 40 seconds to obtain aerosol type in one site by using the Gaussian algorithm.

455 **4.2 Aerosol type determination for typical sites**

456 **4.2.1 Dust aerosol**

457 Figure 7 shows the aerosol types obtained using the new hybrid algorithm for the
458 five sites selected for dust aerosol identification. According to the prediction by the new
459 hybrid algorithm, the aerosols at these five sites mainly contained dust aerosols along
460 with a small amount of U/I, mixed-fine, and BB aerosols, and a large amount of mixed

461 coarse aerosols. This shows that other types of aerosols invaded these areas besides dust
 462 aerosol. BB aerosols may have been transferred from the southern African savannah.
 463 Additionally, U/I aerosols could be from industrial cities, such as Dakar, Abidjan, and
 464 Lagos, which are dominated by anthropogenic aerosols and are close to the AERONET
 465 sites.



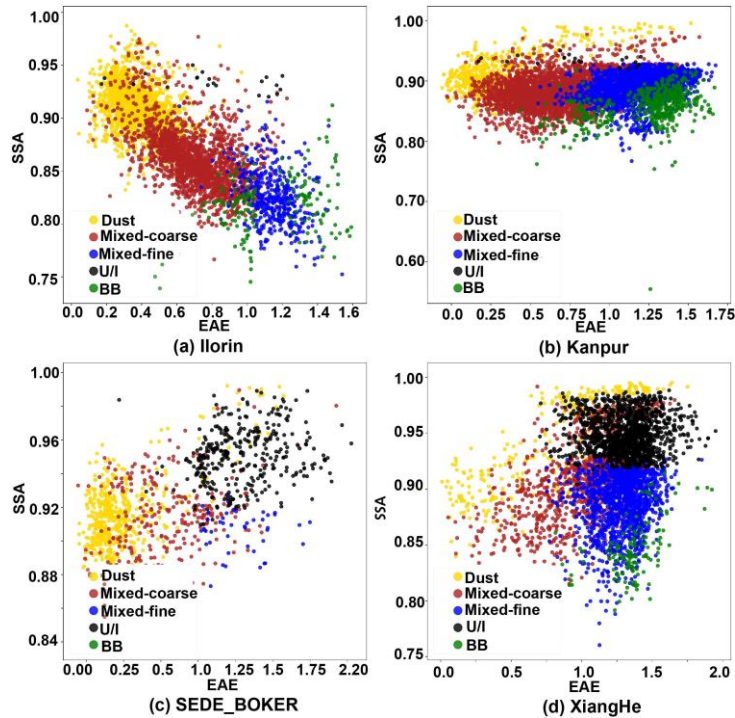
466
 467 **Figure 7.** Identification of dust aerosol at dominant aerosol sites.

468 **4.2.2 Mixed aerosol**

469 Besides Ilorin in Africa, the mixed aerosol AERONET sites, including Kanpur,
 470 Sede_Boker, and XiangHe, are in Asia. The aerosol types at these four sites were
 471 determined using the new hybrid algorithm (Figure 8). Mixed coarse aerosols
 472 dominated the Kanpur, Ilorin, and Sede_Boker sites, and mixed fine aerosols dominated
 473 XiangHe. Part of the dust in Xianghe could be due to the Takla Desert in spring and the
 474 westerly winds prevailing in western China, which transported dust aerosols over long
 475 distances. Additionally, the U/I aerosol in Xianghe could be a result of human activities,
 476 construction emissions, and fuel burning in winter. The BB aerosol was traced to the
 477 burning of a small amount of biomass in Xianghe, located in a suburban area.

478 Furthermore, excluding dust aerosols, we observed BB and U/I aerosols in the
 479 Kanpur site in the Ganges Basin of India. A certain amount of U/I and dust aerosols

480 were also observed in Sede_Boker, located in the industrial center of Israel, possibly
 481 from the Arabian desert. Lastly, Ilorin had the most dust and least BB aerosols because
 482 it is located in central Africa, often affected by the Saharan Desert and African savannah.



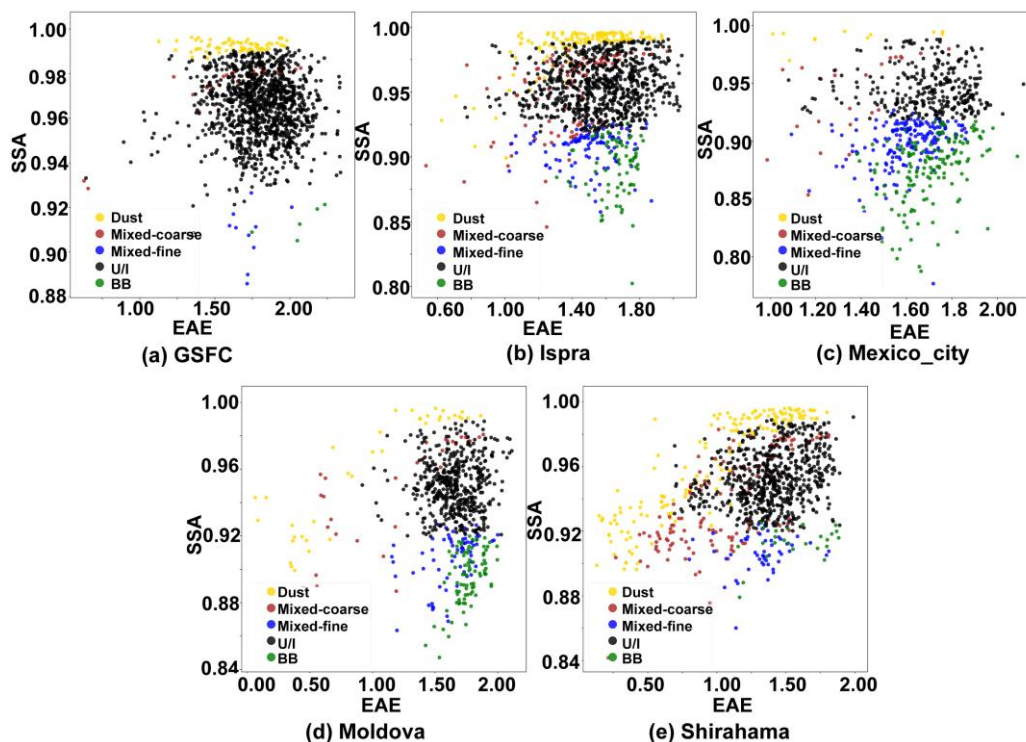
483
 484 **Figure 8.** Same as Figure 7 but for Mixed aerosol.

485 4.2.3 Urban/industrial aerosol

486 All the selected AERONET sites for evaluating the performance of the new hybrid
 487 algorithm in terms of U/I aerosol identification are in Europe or North America (Figure
 488 9). GSFC is located in the densely populated and industrially developed area of
 489 Washington in the United States, explaining its complex aerosol type dominated by the
 490 U/I aerosol followed by a few mixed and BB aerosols and a small amount of dust
 491 aerosols.

492 Ispra is in Turin, one of Italy's largest industrial centers. However, dust-type
 493 aerosols were identified, possibly transported from the Libyan desert when Italian
 494 winters were controlled by southwesterly winds. Moreover, Mexico, where the Mexico
 495 City site is located, is an industrialized country with modern industries and agriculture,
 496 abundant oil production, and a dense population. Nevertheless, we identified dust,
 497 mixed coarse, and BB aerosols in this site using the new hybrid algorithm. These

498 aerosol types could be from the Chihuahuan Desert, an inland desert covering 12% of
 499 Mexico's area and a major source of coarse and dust aerosols. Additionally, the literature
 500 shows that Mexico City is surrounded by forested mountains, which experience many
 501 wildfires during the dry period between November and May; this accounts for BB
 502 aerosols in Mexico City (Yokelson et al. 2007). Finally, the BB aerosols identified at
 503 the Moldova site could be attributed to its rich vegetation cover.

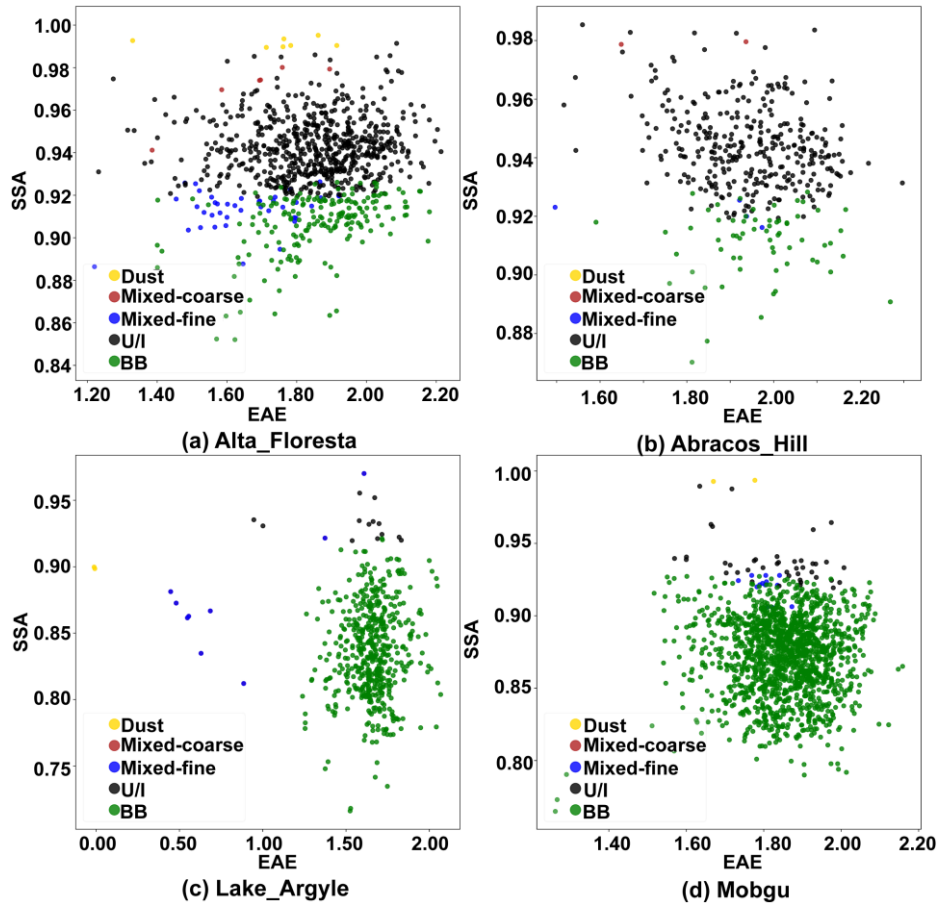


504
 505 **Figure 9.** Same as Figure 8 but for urban/industrial aerosol.

506 4.2.4 Biomass burning aerosol

507 The selected sites were mainly located in the mountains and highlands. Figure 10
 508 shows the aerosol types identified using the new hybrid algorithm. Large amounts of
 509 BB aerosols were identified at all sites. Additionally, a small amount of dust and mixed-
 510 coarse aerosols were identified at the Alta_Floresta site, transported over a long distance
 511 from the Patagonian Desert in Argentina, in southern South America. Moreover, the city
 512 where the site is located is industrially developed and has a large population; therefore,
 513 more U/I aerosols were identified using the new hybrid algorithm. The geographically
 514 close Abracos_Hill and Alta_Floresta sites were characterized by the same aerosol type
 515 and source. Furthermore, one data point in Lake Argyle was classified as a dust aerosol.

516 This means that, although the site is located on the Kimberley Plateau, Australia has a
 517 large desert area, and coarse aerosols still exist. Lastly, a few U/I and several dust-type
 518 aerosols were identified at the Mongu site, possibly caused by aerosol emissions from
 519 nearby cities and dust transport from the Saharan Desert.



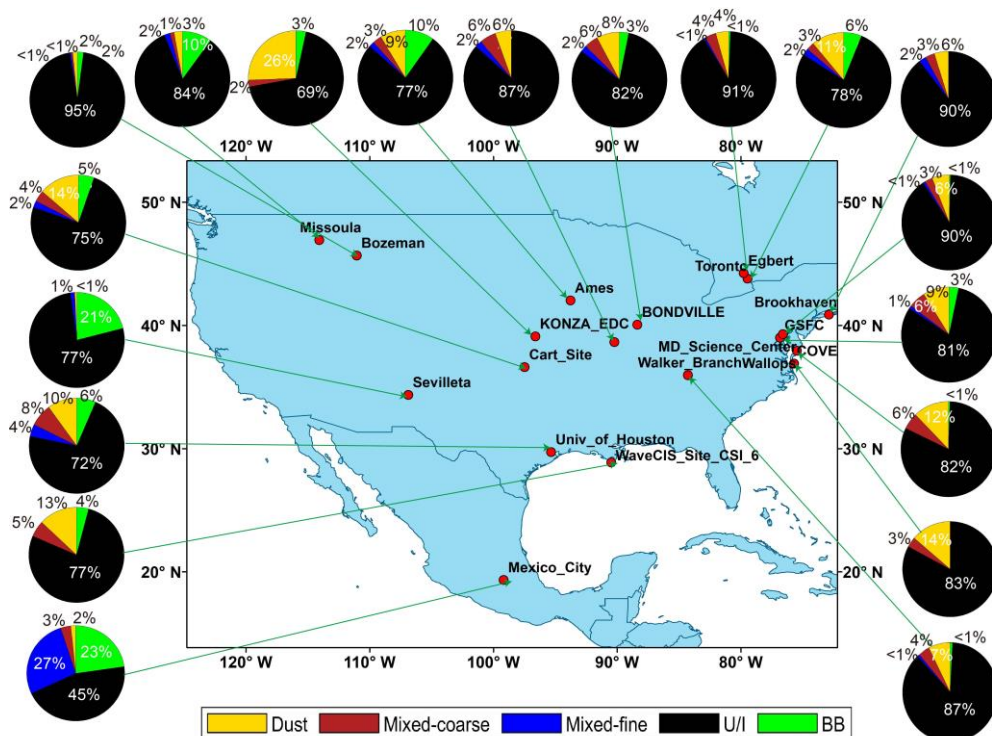
520
 521 **Figure 10.** Same as Figure 9 but for BB aerosol.

522 4.3 Aerosol type distribution on a global scale

523 Given the advantages and accuracy of the new hybrid algorithm in identifying
 524 aerosol types, we used it to divide the data of AERONET sites in different regions of
 525 the world to obtain global aerosol type distribution information. The aerosol types of
 526 each continent are shown in Figures 11-15. Additionally, Figure 16 shows the global
 527 aerosol-type distribution. Notably, the pie chart was placed on each site in the study,
 528 which is a "point source" assessment of the aerosol type and does not represent the
 529 entire region (the size of the pie chart is independent of the optical properties).
 530 Moreover, the sites were screened, and only those with valid data of > 100 aerosol types

531 were considered; however, offshore sites and sites classified as marine aerosol-
 532 dominated by other literature were excluded.

533 Figure 11 shows pie charts of the aerosol types for each scanned AERONET site in
 534 North America. The U/I aerosols, particularly in most mid-eastern regions, contained
 535 mixed and small amounts of biomass aerosols. Additionally, the AERONET sites in
 536 large cities, such as Chicago, New York, Toronto, Ottawa, and Boston, had U/I aerosols.
 537 Many studies have shown that dust aerosols from the Saharan Desert can cross the
 538 Atlantic Ocean to North America in summer. Moreover, there is an inland desert in
 539 western North America, the Chihuahua Desert, responsible for a small amount of dust
 540 and mixed aerosols at the AERONET sites in North America. Additionally, wildfires in
 541 western North America and household wood burning contribute to most BB aerosols
 542 yearly. The central region site is affected by the environment, with an increased
 543 proportion of BB aerosols, and U/I aerosols are still prevalent because the site is located
 544 in a large city and is densely populated.

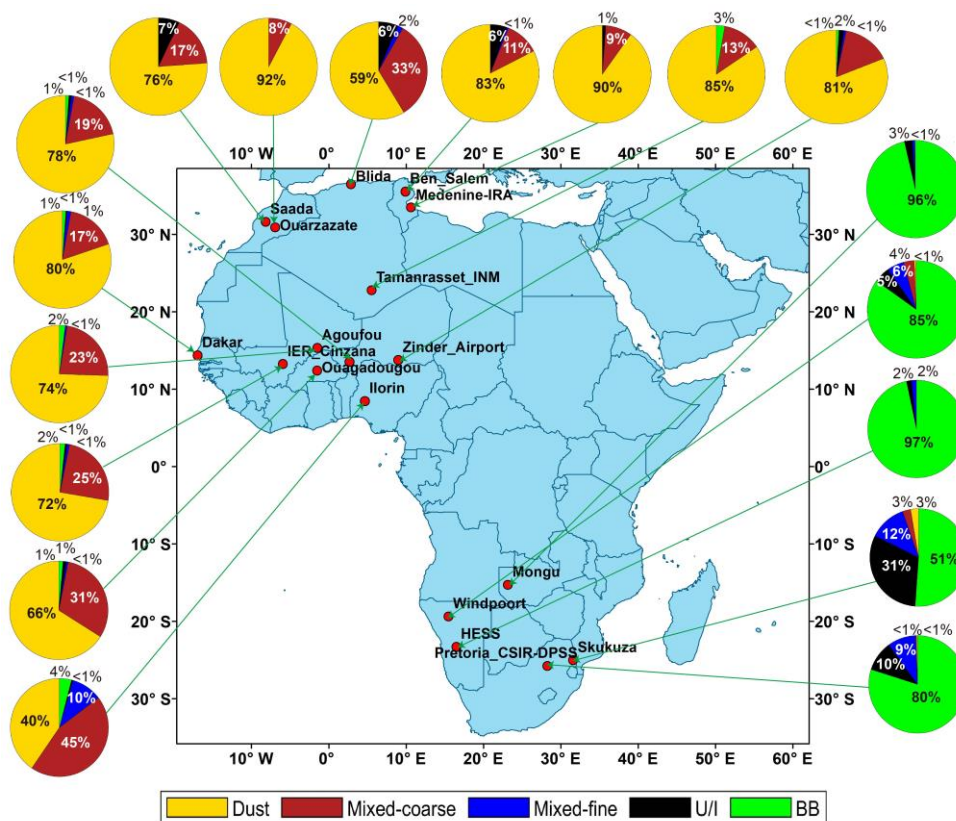


545

546 **Figure 11.** Pie charts of the aerosol types at the major sites of North American.

547 Figure 12 shows the aerosol types in Africa. Northern Africa has the largest desert
 548 in the world, the Saharan Desert; therefore, dust aerosols dominate north of the equator

549 in Africa. However, some AERONET sites in the Sudanese steppe were primarily BB,
 550 with some U/I aerosols in nearby urban sites. The Ilorin site is a typical mixed aerosol
 551 site close to the equator with a small amount of BB aerosols. Most sites close to the
 552 Atlantic coast were affected by dust aerosols, even those on the islands of Capo_Verde.
 553 The reliability of the new model in distinguishing U/I and BB aerosols is demonstrated.
 554 Sites in Southern Africa, such as Namibia, Botswana, and Zambia, are dominated by
 555 BB aerosols. Nevertheless, studies have shown the presence of U/I aerosols at sites in
 556 the urban areas of South Africa. Although U/I and BB aerosols are difficult to
 557 distinguish, the two can be identified in the context of a large urban population and less
 558 biomass combustion, thus establishing the model's accuracy.

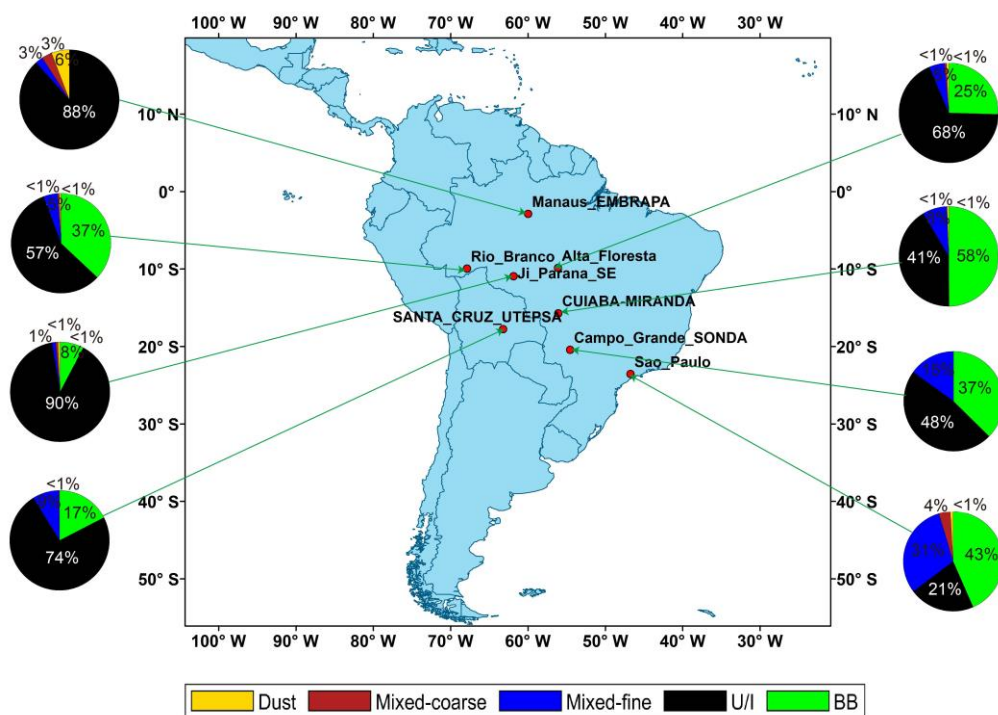


559

560 **Figure 12.** Same as Figure 11 but for Africa.

561 The aerosol types in South America are shown in Figure 13. Here, only eight sites
 562 met the requirement for valid data >100 aerosol types. South America is mainly
 563 dominated by mountainous plateaus, and under the influence of the Brazilian warm
 564 current, many tropical rainforests are distributed in the south; therefore, the background
 565 aerosols are mainly BB aerosols. As shown in Figure 13, large cities, such as Rio Branco,

566 Campo Grande, Manaus, Santa Cruz, and São Paulo, showed an increased proportion
 567 of anthropogenic and mixed aerosols because of their large population and developed
 568 industries. Due to the tropical rainforest climate in southern South America, the
 569 proportion of BB aerosols increased, such as that at the Cuiaba site near the Amazon
 570 River. Additionally, the Manaus site contained a small amount of dust aerosols that were
 571 presumably transported across the Atlantic Ocean from African dust at the same latitude.

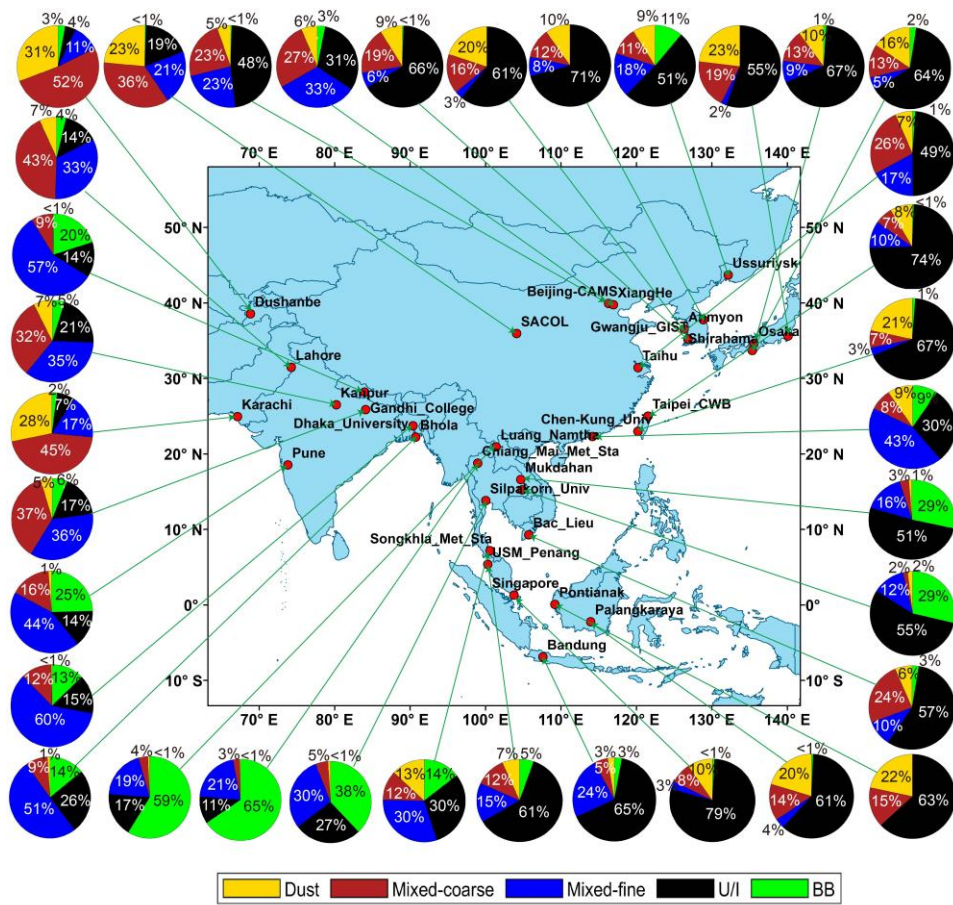


572

573 **Figure 13.** Same as Figure 11 but for South America.

574 The aerosol types in Asia are shown in Figure 14. In western Asia, influenced by
 575 the Indian Desert, sites on the Indian Peninsula were dominated by coarse-particle
 576 aerosols, including dust and mixed coarse aerosols. Kanpur and Pune are densely
 577 populated cities in India, with more mixed-fine aerosols produced by human activities.
 578 Additionally, in Southeast Asia, all sites contained BB aerosols, consistent with Hamill
 579 (2014). This is because of the abundance of tropical rainforests in Southeast Asia.
 580 Moreover, some urban sites, such as Singapore and Penang, had large numbers of U/I
 581 and mixed-fine aerosols. The coastal areas of East Asia, which are densely populated
 582 and industrially developed, were mainly dominated by U/I aerosols. Moreover, dust

583 aerosols appeared at these sites due to dust transported from the Taklamakan Desert in
 584 East Asia.

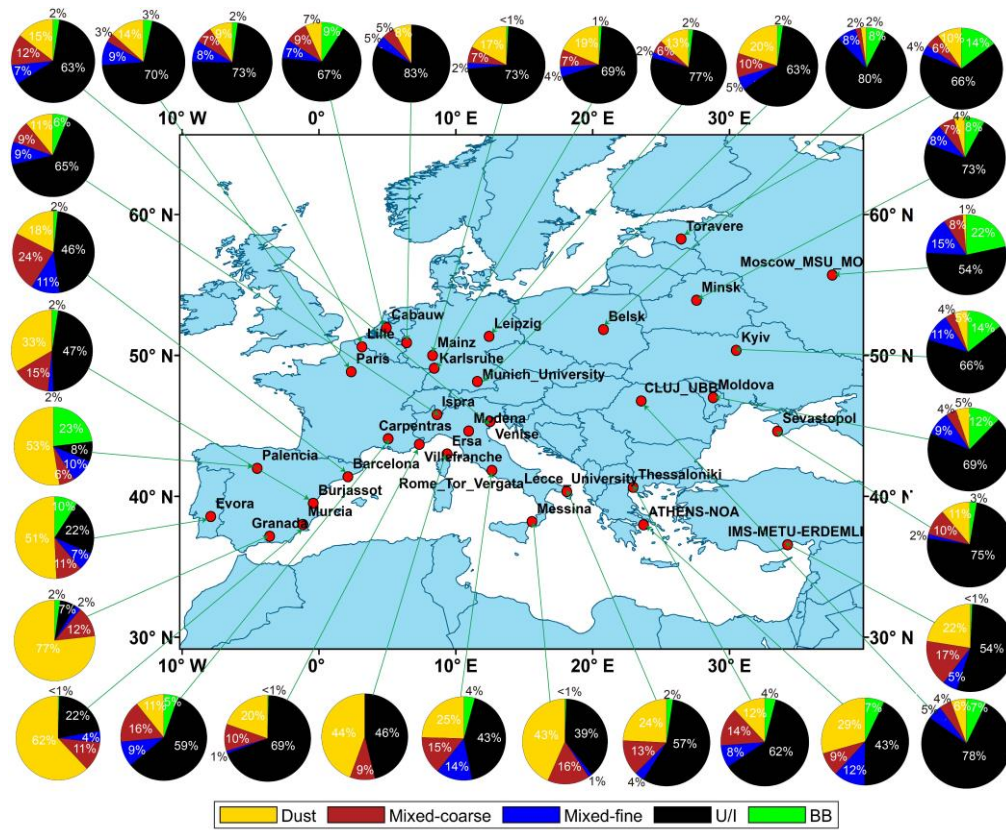


585
 586 **Figure 14.** Same as Figure 11 but for Asia.

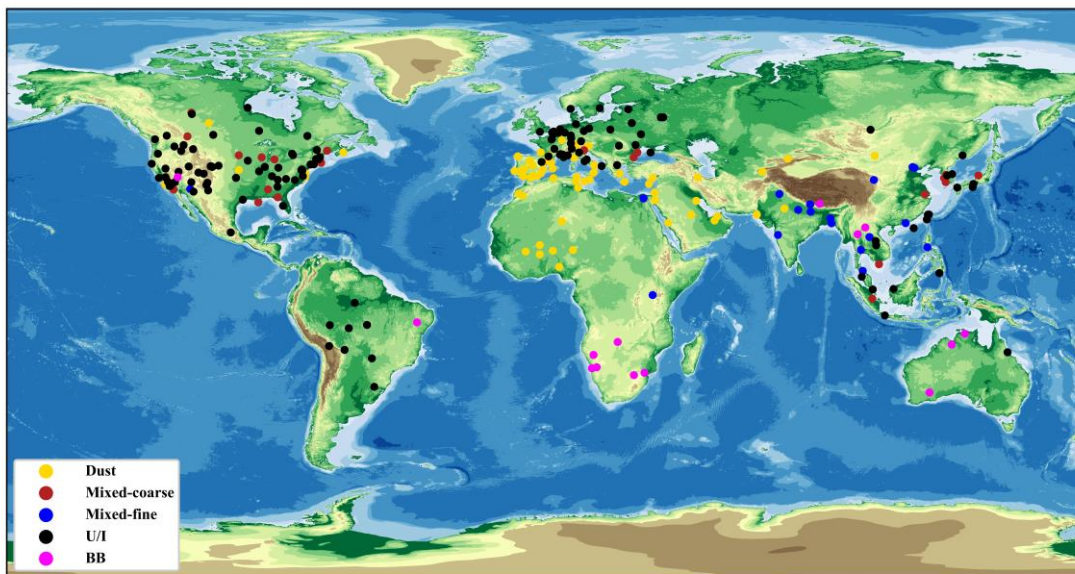
587 The inland areas of East Asia have a smaller population than the coastal areas;
 588 therefore, the proportion of U/I aerosols was small, and that of mixed aerosols was high.
 589 Generally, mixed aerosols are more easily overestimated than U/I aerosols; however,
 590 the new hybrid algorithm identified a larger proportion of U/I aerosols than mixed
 591 aerosols at Asian sites. Therefore, this new hybrid algorithm can be considered for
 592 improving the classification of mixed aerosols versus U/I aerosols.

593 Similarly, southern Europe, which is close to the Saharan and Arabian deserts, was
 594 dominated by dust aerosols, with small amounts of mixed and U/I aerosols. Northern
 595 European sites have many cities and a large population; therefore, the aerosol type was
 596 mainly U/I aerosols, identified using the new hybrid algorithm (Figure 15). Additionally,
 597 small amounts of BB aerosols were identified at most sites in Europe because of olive
 598 groves in agricultural lands in the EU, which produce 91% of the world's olive oil

599 (Lopez-Pineiro et al., 2011). Papadakis et al. (2015) suggested that the biomass
 600 produced from olive oil is used for heating and industry, and its combustion produces
 601 carbonaceous aerosols, considered the major source of fine particle aerosols in Europe
 602 during winter (Puxbaum et al., 2007).



603
 604 **Figure 15.** Same as Figure 11 but for Europe.



605
 606 **Figure 16.** Global dominant aerosol type distribution based on AERONET sites.

607 The global distribution of dominant aerosols in the AERONET site is shown in
608 Figure 16. The graph does not include marine aerosols. There are more aerosol sites on
609 the global map than those on each continent because AERONET sites with > 5 years of
610 data were selected for the global map; however, sites with > 100 valid data points were
611 required for each continent. The global distribution map shows that many BB aerosols
612 were distributed between 20°N and 20°S. This is because this region has a
613 predominantly tropical rainforest climate, with many tropical rainforests and more
614 carbon-containing aerosol emissions. This finding is consistent with those from
615 previous studies that found that global BB aerosols mainly originate from Africa
616 (approximately 52%), followed by South America (approximately 15%), equatorial
617 Asia (approximately 10%), boreal forests (approximately 9%), and Australia
618 (approximately 7%) (Van G. R. et al., 2010). Furthermore, the global distribution map
619 shows a clear distribution band of dust aerosols between 5°N and 35°N, originating
620 from the Saharan Desert in Africa and the Saudi Arabian Desert in Western Asia, which
621 are transported across the ocean to other regions.

622 **5. Conclusion**

623 We developed a new hybrid algorithm to support the rapid classification of aerosol
624 types by building an aerosol optical database for global AERONET sites. This hybrid
625 algorithm is a complex aerosol-type processing algorithm that effectively integrates
626 machine learning and density clustering algorithms. Additionally, this algorithm is not
627 limited by the amount of data and improves the accuracy of aerosol-type classification.
628 On investigating the aerosol types at specific sites with dominant aerosols, we observed
629 that different sites contained one or more aerosol types, with the composition of some
630 specific dominant aerosol sites being more complex than that of others. The new
631 algorithm showed a higher accuracy than that shown by algorithms used in previous
632 studies in identifying aerosol types at specific sites, particularly in distinguishing
633 between U/I and mixed-fine aerosols. Finally, the recognition results of the new hybrid
634 algorithm were closer to the baseline CRI, confirming that the new hybrid algorithm is

635 better than the density-clustering algorithm. On investigating the aerosol types at global
636 sites across the continents using the new algorithm, we observed the dominance of
637 different types of aerosols at different sites, and the composition of these could be
638 logically and effectively attributed to the geographical location, energy consumption
639 structure, meteorological conditions and activities happening at the respective sites.

640 In this study, the existing aerosol type identification algorithm was improved using
641 global ground-based AERONET optical property parameter data, and the spatial
642 distribution characteristics of global aerosol types were analyzed, which impacted
643 aerosol radiation research and optical thickness inversion accuracy. Additionally, the
644 presumption of spherical dust aerosols in the Mie scattering model diverges from their
645 actual non-spherical nature in the environment, introducing potential inaccuracies. The
646 optical database's precision, therefore, necessitates further refinement. Future
647 advancements could involve adopting more potent machine learning techniques, such
648 as advanced algorithms beyond the current random forest method. Meanwhile, multi-
649 source satellite data and reanalysis products can be incorporated into aerosol-type
650 identification. Ultimately, this study will provide support for the identification and
651 control of air pollution sources.

652 **Author contributions**

653 **Feng Zhang** designed the study. **Xiaoli Wei** analyzed the results and wrote the original
654 draft. **Qian Cui** engaged in data processing, manuscript editing, and restructuring.
655 **Leiming Ma** revised the paper and gave constructive suggestions. **Wenwen Li** gave
656 constructive comments on the paper. **Peng Liu** revised the paper. All authors
657 contributed to the study.

658 **Competing interests**

659 The authors declare that they have no conflict of interest.

660 **Acknowledgments**

661 This work was supported by the National Key R&D Program (2021YFB3900401),

662 the National Natural Science Foundation of China (42075125 and 42105081) and
663 Science and Technology Foundation of Shanghai (23ZR1454100)

664 **References**

- 665 Van G. R., der W., Randerson, J. T., Giglio, L., Collatz, G. J., Mu, M., Kasibhatla, P. S., Morton, D. C.,
666 Defries, R. S., Jin, Y., and Van Leeuwen, T. T.: Global fire emissions and the contribution of
667 deforestation, savanna, forest, agricultural, and peat fires (1997–2009), *Atmos. Chem. Phys.*, 10,
668 11707–11735, <https://doi.org/10.5194/acp-10-11707-2010>, 2010.
- 669 Bahadur, R., Praveen, P. S., Xu, Y., and Ramanathan, V.: Solar absorption by elemental and brown carbon
670 determined from spectral observations, *Proc. Natl. Acad. Sci. U. S. A.*, 109, 17366–17371,
671 <https://doi.org/10.1073/pnas.1205910109>, 2012.
- 672 Bian, Yuxuan et al.: Development and Validation of a CCD-Laser Aerosol Detective System for
673 Measuring the Ambient Aerosol Phase Function., *Atmospheric measurement techniques*, 10 (6),2313–
674 2322. <https://doi.org/10.5194/amt-10-2313>, 2017
- 675 Boselli, A., Caggiano, R., Cornacchia, C., Madonna, F., Mona, L., Macchiato, M., Pappalardo, G., and
676 Trippetta, S.: Multi year sun-photometer measurements for aerosol characterization in a Central
677 Mediterranean site, *Atmos. Res.*, 104–105, 98–110, <https://doi.org/10.1016/j.atmosres.2011.08.002>,
678 2012.
- 679 Breiman: Random forests, *Machine Learning*, 45(1), 5–32, <https://doi.org/10.1023/A:1010933404324>,
680 2001.
- 681 Che, H., Bing, Q., Zhao, H., Xia, X., and Zhang, X.: Aerosol optical properties and direct radiative
682 forcing based on measurements from the China Aerosol Remote Sensing Network (CARSNET) in
683 eastern China, *Atmos. Chem. Phys.*, 18, 405–425, <https://doi.org/10.5194/acp-18-405-2018>, 2018.
- 684 Choi, W., Lee, H., and Park, J.: A first approach to aerosol classification using space-borne measurement
685 data: Machine learning-based algorithm and evaluation, *Remote Sens.*, 13, 1–21,
686 <https://doi.org/10.3390/rs13040609>, 2021a.
- 687 Choi, W., Lee, H., Kim, D., and Kim, S.: Improving spatial coverage of satellite aerosol classification
688 using a random forest model, *Remote Sens.*, 13 (7):1268. <https://doi.org/10.3390/rs13071268>,2021b.
- 689 Dubovik, O. and King, M. D.: A flexible inversion algorithm for retrieval of aerosol optical properties
690 from Sun and sky radiance measurements, *J. Geophys. Res. Atmos.*, 105, 20673–20696,
691 <https://doi.org/10.1029/2000JD900282>, 2000.
- 692 Dubovik, O., Holben, B., Eck, T. F., Smirnov, A., Kaufman, Y. J., King, M. D., Tanré, D., and Slutsker,
693 I.: Variability of absorption and optical properties of key aerosol types observed in worldwide locations,
694 *J. Atmos. Sci.*, 59, 590–608, <https://doi.org/10.1175/1520-0469>, 2002.
- 695 Eck, T. F., Holben, B. N., Reid, J. S., Dubovik, O., Smirnov, A., O’Neill, N. T., Slutsker, I., and Kinne,
696 S.: Wavelength dependence of the optical depth of biomass burning, urban, and desert dust aerosols,
697 *J. Geophys. Res. Atmos.*, 104, 31333–31349, <https://doi.org/10.1029/1999JD900923>, 1999.
- 698 Elham Ghasemifar.:Climatology of aerosol types and their vertical distribution over Iran using CALIOP
699 dataset during 2007–2021,*Remote Sensing Applications: Society and Environment*,32, 101053, 2352-
700 9385,<https://doi.org/10.1016/j.rsase.2023.101053>.2023.
- 701 Fernandez-Delgado, M., Cernadas, E., Barro, S., and Amorim, D.: Do we Need Hundreds of Classifiers
702 to Solve Real World Classification Problems?, *J. Mach. Learn. Res.*, 15, 3133–3181,
703 <https://dl.acm.org/doi/10.5555/2627435.2697065>, 2014.

704 Fu, Q., Thorsen, T.J., Su, J., Ge, J., & Huang, J.: Test of Mie-based single-scattering properties of non-
705 spherical dust aerosols in radiative flux calculations. *Journal of Quantitative Spectroscopy & Radiative*
706 *Transfer*, 110, 1640-1653. <https://doi.org/10.1016/j.jqsrt.2009.03.010>, 2009

707 Giles, D. M., Holben, B. N., Eck, T. F., Sinyuk, A., Smirnov, A., Slutsker, I., Dickerson, R. R., Thompson,
708 A. M., and Schafer, J. S.: An analysis of AERONET aerosol absorption properties and classifications
709 representative of aerosol source regions, *J. Geophys. Res. Atmos.*, 117, 1–16,
710 <https://doi.org/10.1029/2012JD018127>, 2012.

711 Hamill, P., Giordano, M., Ward, C., Giles, D., and Holben, B.: An AERONET-based aerosol classification
712 using the Mahalanobis distance, *Atmos. Environ.*, 140, 213–233,
713 <https://doi.org/10.1016/j.atmosenv.2016.06.002>, 2016.

714 Kalapureddy, M. C. R., Kaskaoutis, D. G., Ernest Raj, P., Devara, P. C. S., Kambezidis, H. D.,
715 Kosmopoulos, P. G., and Nastos, P. T.: Identification of aerosol type over the Arabian Sea in the
716 premonsoon season during the Integrated Campaign for Aerosols, Gases and Radiation Budget
717 (ICARB), *J. Geophys. Res. Atmos.*, 114, 1–12, <https://doi.org/10.1029/2009JD011826>, 2009.

718 Kaskaoutis, D. G., Kharol, S. K., Sinha, P. R., Singh, R. P., Badarinath, K., Mehdi, W., and Sharma, M.:
719 Contrasting aerosol trends over South Asia during the last decade based on MODIS observations,
720 *Atmos. Meas. Tech. Discuss.*, 4, 5275–5323, <https://doi.org/10.5194/amtd-4-5275-2011>, 2011.

721 Kiehl, J. T. and Briegleb, B. P.: The relative roles of sulfate aerosols and greenhouse gases in climate
722 forcing, *Science* (80-.), 260, 311–314, <http://dx.doi.org/10.1126/science.260.5106.311>, 1993.

723 Kumar, K. R., Kang, N., and Yin, Y.: Classification of key aerosol types and their frequency distributions
724 based on satellite remote sensing data at an industrially polluted city in the Yangtze River Delta, China,
725 *Int. J. Climatol.*, 38, 320–336, <https://doi.org/10.1002/joc.5178>, 2018.

726 Lee, J., Kim, J., Song, C. H., Kim, S. B., Chun, Y., Sohn, B. J., and Holben, B. N.: Characteristics of
727 aerosol types from AERONET sunphotometer measurements, *Atmos. Environ.*, 44, 3110–3117,
728 <https://doi.org/10.1016/j.atmosenv.2010.05.035>, 2010.

729 Levy, R. C., Remer, L. A., Mattoo, S., Vermote, E. F., and Kaufman, Y. J.: Second-generation operational
730 algorithm: Retrieval of aerosol properties over land from inversion of Moderate Resolution Imaging
731 Spectroradiometer spectral reflectance, *J. Geophys. Res. Atmos.*, 112,
732 <https://doi.org/10.1029/2006JD007811>, 2007.

733 Li, K., Bai, K., Ma, M., Guo, J., Li, Z., Wang, G., and Chang, N. Bin: Spatially gap free analysis of
734 aerosol type grids in China: First retrieval via satellite remote sensing and big data analytics, *ISPRS J.*
735 *Photogramm. Remote Sens.*, 193, 45–59, <https://doi.org/10.1016/j.isprsjprs.2022.09.001>, 2022.

736 Lin, J., Zheng, Y., Shen, X., Xing, L., and Che, H.: Global aerosol classification based on aerosol robotic
737 network (Aeronet) and satellite observation, *Remote Sens.*, 13, 1–23,
738 <https://doi.org/10.3390/rs13061114>, 2021.

739 Ma Lin.: Measurement of aerosol size distribution function using Mie scattering - Mathematical
740 considerations., *Journal of aerosol science*, 38(11),1150-1162,
741 <https://doi.org/10.1016/j.jaerosci.2007.08.003>, 2007.

742 Lopez-Pineiro, A., Cabrera, D., Albarran, A., and Pefia, D.: Influence of two-phase olive mill waste
743 application to soil on terbuthylazine behaviour and persistence under controlled and field conditions,
744 *J. Soils Sediments*, 11, 771–782, <https://doi.org/10.1007/s11368-011-0362-3>, 2011.

745 Lu, F., Chen, S., Hu, Z., Han, Z., Alam, K., Luo, H., Bi, H., Chen, J., and Guo, X.: Sensitivity and
746 uncertainties assessment in radiative forcing due to aerosol optical properties in diverse locations in
747 China, *Sci. Total Environ.*, 860, 160447, <https://doi.org/10.1016/j.scitotenv.2022.160447>, 2023.

748 Michael, I., Mishchenko, and, Larry, D., and Travis: Light scattering by polydisperse, rotationally
749 symmetric nonspherical particles: Linear polarization, *J. Quant. Spectrosc. Radiat. Transf.*,
750 [https://doi.org/10.1016/0022-4073\(94\)90130-9](https://doi.org/10.1016/0022-4073(94)90130-9), 1994.

751 Moraes, C. P. A., Fantinato, D. G., and Neves, A.: Epanechnikov kernel for PDF estimation applied to
752 equalization and blind source separation, *Signal Processing*, 189, 108251,
753 <https://doi.org/10.1016/j.sigpro.2021.108251>, 2021.

754 Nandan, R., Ratnam, M.V., Kiran, V.R., Madhavan, B.L., & Naik, D.N.: Estimation of Aerosol Complex
755 Refractive Index over a tropical atmosphere using a synergy of in-situ measurements. *Atmospheric
756 Research*, 257, 105625, <https://doi.org/10.1016/J.ATMOSRES.2021.105625>, 2021
757 Nicolae, D., Vasilescu, J., Talianu, C., Biniotoglou, I., Nicolae, V., Andrei, S., and Antonescu, B.: A neural network
758 aerosol-typing algorithm based on lidar data, *Atmos. Chem. Phys.*, 18, 14511–14537,
759 <https://doi.org/10.5194/acp-18-14511-2018>, 2018.

760 Omar, A. H., Won, J. G., Winker, D. M., Yoon, S. C., Dubovik, O., and McCormick, M. P.: Development
761 of global aerosol models using cluster analysis of Aerosol Robotic Network (AERONET)
762 measurements, *J. Geophys. Res. D Atmos.*, 110, 1–14, <https://doi.org/10.1029/2004JD004874>, 2005.

763 Pace, G., di Sarra, A., Meloni, D., Piacentino, S., and Chamard, P.: Aerosol optical properties at
764 Lampedusa (Central Mediterranean). 1. Influence of transport and identification of different aerosol
765 types, *Atmos. Chem. Phys.*, 6, 697–713, <https://doi.org/10.5194/acp-6-697-2006>, 2006.

766 Papadakis, G. Z., Megaritis, A. G., and Pandis, S. N.: Effects of olive tree branches burning emissions
767 on PM_{2.5} concentrations, *Atmos. Environ.*, 112, 148–158,
768 <https://doi.org/10.1016/j.atmosenv.2015.04.014>, 2015.

769 Pathak, B., Bhuyan, P. K., Gogoi, M., and Bhuyan, K.: Seasonal heterogeneity in aerosol types over
770 Dibrugarh-North-Eastern India, *Atmos. Environ.*, 47, 307–315,
771 <https://doi.org/10.1016/j.atmosenv.2011.10.061>, 2012.

772 Pawar, G. V., Devara, P. C. S., and Aher, G. R.: Identification of aerosol types over an urban site based
773 on air-mass trajectory classification, *Atmos. Res.*, 164–165, 142–155,
774 <https://doi.org/10.1016/j.atmosres.2015.04.022>, 2015.

775 Puxbaum, H., Caseiro, A., Sánchez-Ochoa, A., Kasper-Giebl, A., Claeys, M., Gelencsér, A., Legrand, M.,
776 Preunkert, S., and Pio, C.: Levoglucosan levels at background sites in Europe for assessing the impact
777 of biomass combustion on the European aerosol background, *J. Geophys. Res.*, 112, D23S05,
778 <https://doi.org/10.1029/2006JD008114>, 2007.

779 Quirantes, Arturo et al.: Extinction-related Angström exponent characterization of submicrometric
780 volume fraction in atmospheric aerosol particles., *Atmospheric Research*, 228(D24), 270-280,
781 <https://doi.org/10.1016/j.atmosres.2019.06.009>, 2019

782 Ramanathan, V., Crutzen, P. J., Lelieveld, J., Mitra, A. P., Althausen, D., Anderson, J., Andreae, M. O.,
783 Cantrell, W., Cass, G. R., and Chung, C. E.: Indian Ocean Experiment: An integrated analysis of the
784 climate forcing and effects of the great Indo-Asian haze, *J. Geophys. Res. Atmos.*, 106,
785 <https://doi.org/10.1029/2001JD900133>, 2001.

786 Raut, J. C. and Chazette, P.: Radiative budget in the presence of multi-layered aerosol structures in the
787 framework of AMMA SOP-0, *Atmos. Chem. Phys.*, 8, 6839–6864, <https://doi.org/10.5194/acp-8-6839-2008>, 2008.

789 Reddy LA, Glover TA, Dudek CM, Alperin A, Wiggs NB, Bronstein B.: A randomized trial examining
790 the effects of paraprofessional behavior support coaching for elementary students with disruptive
791 behavior disorders: Paraprofessional and student outcomes. *J Sch Psychol.* 2022 Jun;92:227-245.

792 <https://doi.org/10.1016/j.jsp.2022.04.002>, 2022. Redemann, J., Turco, R. P., Liou, K. N., Russell, P. B.,
793 Bergstrom, R. W., Schmid, B., Hobbs, P. V., Hartley, W. S., Ismail, S., and Ferrare, R. A.: Retrieving
794 the vertical structure of the effective aerosol complex index of refraction from a combination of aerosol
795 in situ and remote sensing measurements during TARFOX, *J. Geophys. Res.*, 105 (D8), 9949–9970,
796 doi:10.1029/1999JD901044, 2000.

797 Remer, L. A., Tanré, D., and Kaufman, Y. J.: Algorithm for remote sensing of tropospheric aerosol from
798 MODIS: Collection 005, 2009.

799 Rosenblatt, M.: Remarks on Some Nonparametric Estimates of a Density Function, Remarks on Some
800 Nonparametric Estimates of a Density Function. In: Davis, R., Lii, K. S., Politis, D. (eds) Selected
801 Works of Murray Rosenblatt. Selected Works in Probability and Statistics. Springer, New York, NY.
802 https://doi.org/10.1007/978-1-4419-8339-8_13, 2011.

803 Sheridan, P. J., Delene, D. J., and Ogren, J. A.: Four Years of Continuous Surface Aerosol Measurements
804 from the DOE / ARM Southern Great Plains CART Site, 1–8, <https://doi.org/10.1029/2001JD000785>,
805 2001.

806 Shin, S. K., Tesche, M., Noh, Y., and Müller, D.: Aerosol-type classification based on AERONET version
807 3 inversion products, *Atmos. Meas. Tech.*, 12, 3789–3803, <https://doi.org/10.5194/amt-12-3789-2019>,
808 2019.

809 Siomos, N., Fountoulakis, I., Natsis, A., Drosoglou, T., and Bais, A.: Automated aerosol classification
810 from spectral UV measurements using machine learning clustering, *Remote Sens.*, 12, 1–18,
811 <https://doi.org/10.3390/rs12060965>, 2020.

812 Tanré, D., Kaufman, Y. J., Holben, B. N., Chatenet, B., Karnieli, A., Lavenu, F., Blarel, L., Dubovik, O.,
813 Remer, L. A., and Smirnov, A.: Climatology of dust aerosol size distribution and optical properties
814 derived from remotely sensed data in the solar spectrum, *J. Geophys. Res. Atmos.*, 106, 18205–18217,
815 <https://doi.org/10.1029/2000JD900663>, 2001.

816 Tong, H., Lakey, P. S. J., Arangio, A. M., Socorro, J., Kampf, C. J., Berkemeier, T., Brune, W. H., Pöschl,
817 U., and Shiraiwa, M.: Reactive oxygen species formed in aqueous mixtures of secondary organic
818 aerosols and mineral dust influencing cloud chemistry and public health in the Anthropocene, *Faraday*
819 *Discuss.*, 200, 251–270, <https://doi.org/10.1039/c7fd00023e>, 2017.

820 Wang J, Liu Y, Chen L, Liu Y, Mi K, Gao S, Mao J, Zhang H, Sun Y, Ma Z.: Validation and calibration
821 of aerosol optical depth and classification of aerosol types based on multi-source data over China. *Sci*
822 *Total Environ.* 2023 Dec 10;903:166603. doi: 10.1016/j.scitotenv.2023.

823 Wu, Y., Li, J., Xia, Y., Deng, Z., Tao, J., Tian, P., Gao, Z., Xia, X., and Zhang, R.: Size-resolved refractive
824 index of scattering aerosols in urban Beijing: A seasonal comparison, *Aerosol Sci. Technol.*, 55, 1070–
825 1083, <https://doi.org/10.1080/02786826.2021.1924357>, 2021.

826 Yang, M., Howell, S. G., Zhuang, J., and Huebert, B. J.: Attribution of aerosol light absorption to black
827 carbon, brown carbon, and dust in China - Interpretations of atmospheric measurements during EAST-
828 AIRE, *Atmos. Chem. Phys.*, 9, 2035–2050, <https://doi.org/10.5194/acp-9-2035-2009>, 2009.

829 Yokelson, R. J., Urbanski, S. P., Atlas, E. L., Toohey, D. W., Alvarado, E. C., Crounse, J. D., Wennberg,
830 P. O., Fisher, M. E., Wold, C. E., and Campos, T. L.: Emissions from forest fires near Mexico City ,
831 *Atmos. Chem. Phys.*, 7, 5569–5584, <https://doi.org/10.5194/acp-7-5569-2007>, 2007.

832 Yousefi, R., Wang, F., Ge, Q., and Shaheen, A.: Long-term aerosol optical depth trend over Iran and
833 identification of dominant aerosol types, *Sci. Total Environ.*, 722,
834 <https://doi.org/10.1016/j.scitotenv.2020.137906>, 2020.

835 Zhang, L. and Li, J.: Variability of major aerosol types in China classified using AERONET

836 measurements, *Remote Sens.*, 11, <https://doi.org/10.3390/rs11202334>, 2019.

837 Zhao, G., Li, F., & Zhao, C.: Determination of the refractive index of ambient aerosols. *Atmospheric*

838 *Environment*, 240, 117800. <https://doi.org/10.1016/j.atmosenv.2020.117800>,2020

839

840